

Nucleosynthetic yields from neutron stars accreting in binary common envelopes

J. Keegans¹★†, C. L. Fryer^{2,3,4,5}†, S. W. Jones^{6,2}†, B. Côté^{6,7}†, K. Belczynski⁸,
F. Herwig^{6,9}†, M. Pignatari^{1,6,7}†, A. M. Laird¹⁰† and C. Aa. Diget¹⁰

¹*E. A. Milne Center for Astrophysics, University of Hull, Hull HU6 7RX, UK*

²*Computational Physics and Methods Group (CCS-2), Los Alamos National Laboratory, Los Alamos, NM 87544, USA*

³*Department of Astronomy, The University of Arizona, Tucson, AZ 85721, USA*

⁴*Department of Physics and Astronomy, The University of New Mexico, Albuquerque, NM 87131, USA*

⁵*The George Washington University, Washington, DC 20052, USA*

⁶*Joint Institute for Nuclear Astrophysics – Center for the Evolution of the Elements, Notre Dame, IN 46556, USA*

⁷*Konkoly Observatory, Research Center for Astronomy and Earth Sciences, Hungarian Academy of Sciences, Konkoly Thege Miklos ut 15-17, H-1121 Budapest, Hungary*

⁸*Nicolaus Copernicus Astronomical Center, Polish Academy of Sciences, ul. Bartycka 18, PL-00-716 Warsaw, Poland*

⁹*Department of Physics & Astronomy, University of Victoria, Victoria, BC V8P5C2 Canada*

¹⁰*Department of Physics, University of York, Heslington, York YO10 5DD, UK*

Accepted 2019 February 1. Received 2019 January 28; in original form 2018 October 24

ABSTRACT

Massive-star binaries can undergo a phase where one of the two stars expands during its advanced evolutionary stage as a giant and envelops its companion, ejecting the hydrogen envelope and tightening its orbit. Such a common envelope phase is required to tighten the binary orbit in the formation of many of the observed X-ray binaries and merging compact binary systems. In the formation scenario for neutron star binaries, the system might pass through a phase where a neutron star spirals into the envelope of its giant star companion. These phases lead to mass accretion on to the neutron star. Accretion on to these common-envelope-phase neutron stars can eject matter that has undergone burning near to the neutron star surface. This paper presents nucleosynthetic yields of this ejected matter, using population synthesis models to study the importance of these nucleosynthetic yields in a galactic chemical evolution context. Depending on the extreme conditions in temperature and density found in the accreted material, both proton-rich and neutron-rich nucleosynthesis can be obtained, with efficient production of neutron-rich isotopes of low Z material at the most extreme conditions, and proton-rich isotopes, again at low Z , in lower density models. Final yields are found to be extremely sensitive to the physical modelling of the accretion phase. We show that neutron stars accreting in binary common envelopes might be a new relevant site for galactic chemical evolution, and therefore more comprehensive studies are needed to better constrain nucleosynthesis in these objects.

Key words: nuclear reactions, nucleosynthesis, abundances – stars: abundances – gamma-ray burst: general – stars: neutron.

1 INTRODUCTION

A number of dedicated observing programmes have shown that most massive stars are formed in systems with at least one binary companion (Kiminki et al. 2007, 2009; Kobulnicky & Fryer 2007;

Kiminki & Kobulnicky 2012; Sana et al. 2012; Kobulnicky et al. 2014). Those binaries in tight orbits can undergo one or more mass transfer phases where mass from a star, typically as it expands (e.g. in a giant phase) and overfills its Roche lobe, flows on to its companion. If the expansion is faster than the companion can incorporate the overflowing mass, the system can go through a common envelope (CE) phase where the expanding star envelops its companion, causing the core of the expanding star and its companion to share a CE. The CE phase causes the binary to tighten

* E-mail: j.keegans@2016.hull.ac.uk

† NuGrid Collaboration, <http://nugridstars.org>

its orbit and is postulated to explain many of the tight-orbit, massive-star binaries (Ivanova et al. 2013).

In the formation of a variety of massive-star binaries including X-ray binaries and double compact object systems, the stellar system evolves through one, and often two, CE phases. In the first CE phase, the more massive star (primary) evolves off the main sequence, enveloping its companion. In some cases, the resultant tightening of the orbit produces a binary that is sufficiently close that, even after the subsequent collapse and explosion of the primary, the wind of the companion can accrete on to the neutron star. This is a common scenario behind the production of massive X-ray binaries. In some cases, when the companion star evolves off the main sequence, a second CE phase where a neutron star is enveloped by the companion occurs. This can tighten the orbit prior to the supernova explosion of the companion that produces binary pulsar systems and compact binaries that are believed to be the site of short-duration gamma-ray bursts (GRBs; Fryer, Woosley & Hartmann 1999b; Bloom, Sigurdsson & Pols 1999), including merging neutron star systems (Dominik et al. 2012, 2013, 2015) like the one recently detected by advanced LIGO/Virgo (Abbott et al. 2017). If the neutron star (NS) spirals into the core of the companion, it can produce a long-duration GRB, the so-called helium-merger model (Fryer & Woosley 1998).

The ultimate fate of the binary in this CE phase depends on the masses of the stars and the orbital separation at the onset of the phase. Many systems eject the hydrogen envelope, forming a binary consisting of a helium star and a NS. Others do not have sufficient orbital energy to eject the hydrogen envelope prior to merging with the helium core. These helium mergers were initially proposed to be a long-lived giant star powered by a central Eddington-rate accreting neutron star known as a Thorne–Zytlow object (Thorne & Zytlow 1975). However, calculations including neutrino processes found that most of the energy released in the neutron star accretion would be radiated efficiently through neutrinos, allowing the neutron star to accrete at the Bondi–Hoyle rate, causing it to rapidly collapse to a black hole (Fryer, Benz & Herant 1996; Fryer & Woosley 1998).

This helium-merger system, forming a black hole accreting system became one of the proposed black hole accretion disc GRB models (Popham, Woosley & Fryer 1999; Zhang & Fryer 2001). Subsequent simulations have studied the potential of this system to produce ultralong duration gamma-ray bursts or peculiar supernovae (Fryer et al. 2013; Soker & Gilkis 2018).

Material accreting on to neutron stars is not completely incorporated into the neutron star. If the material has enough angular momentum, it can form a disc that could ultimately drive a jet. This is believed to be rare in most CE scenarios (Murguia-Berthier et al. 2017). For neutron star systems, even if the material does not have a sufficient angular momentum to form a disc, some of the accreting material will be reheated and ejected (Fryer et al. 2006; Fryer 2009). During this accretion process, temperatures and densities become so high that both neutrino emission (that can alter the electron fraction) and nuclear burning can significantly alter the composition of the material. For the high accretion rates of supernova fallback, the reheated ejecta can burn into heavy r-process elements (Fryer et al. 2006). Fallback accretion rates range from a few times 10^{-3} to $1 M_{\odot} s^{-1}$. CE accretion rates are typically lower than these rates: ranging from 10^{-4} to $10^6 M_{\odot} yr^{-1}$ (note the former is in per second while the latter is per year).

In this paper, we will study the yields from these lower CE accretion rates. In Section 2 we review NS accretion in CE, estimating accretion rates for a range of stellar models at different phases in the star’s life. In Section 3 we review the range of

yields expected as a function of accretion rate from our single zone models. To determine the effect CE yields have on galactic chemical evolution (GCE), we must calculate the distribution of binaries and CE scenarios. By using these distributions and stellar models, we can estimate the accretion rates. In Section 4.1, we use binary population systems to study yields from stars and stellar populations. We conclude in Section 5 with a discussion of the role these yields play in GCE.

2 NS ACCRETION IN CE EVOLUTION

2.1 Estimating mass accretion

When a massive-star companion in a binary with an NS overfills its Roche lobe, its material accretes on to the neutron star. The accretion rate can be much faster than the NS can incorporate, ultimately developing into a CE phase. A number of assumptions are made in estimating this accretion rate and, especially for NSs, there seems to be some confusion on the validity of these assumptions. Here we review the basic physics assumptions and approximations used in this paper to estimate accretion rates. In astrophysics, the standard estimate for accretion on to a point source is the Bondi–Hoyle–Littleton solution (Hoyle & Lyttleton 1941; Bondi 1952). The Bondi radius (R_B) for a neutron star of mass (M_{NS}) can be determined by the radius that material of velocity v is bound to the NS, i.e.:

$$v^2/R_B = GM_{NS}/R_B^2 \rightarrow R_B = GM_{NS}/v^2, \quad (1)$$

where G is the gravitational constant. In the simplest case, v is set to the sound speed (c_s). But if the NS is moving with respect to the material, the relative motion (v_m) should also be included. One simple, and often standard, way to include both velocities is through a quadratic sum: $v = \sqrt{v_m^2 + c_s^2}$:

$$R_B = 2 GM_{NS}/(c_s^2 + v_m^2). \quad (2)$$

The accretion rate is roughly the mass within this Bondi radius divided by the free-fall time at this radius. More accurately, this accretion rate is

$$\dot{M}_B = \lambda_{BHL} 4\pi R_B^2 \rho v, \quad (3)$$

where ρ is the density of the ambient medium and λ_{BHL} is a non-dimensional parameter: $\lambda_{BHL} = 2/(3\pi)$ if we assume free-fall. Calculations of Bondi–Hoyle accretion allow refinement of the value for λ_{BHL} and determination of the accuracy of our solution to include the different velocity terms (Ruffert 1994a). In scenarios like our CE phase, there is both a velocity and density gradient across the Bondi radius, and these features drive instabilities in the accretion that can decrease the accretion rate (Ruffert 1994b; Ruffert & Arnett 1994; MacLeod & Ramirez-Ruiz 2014; MacLeod & Ramirez-Ruiz 2015; MacLeod et al. 2017; Murguia-Berthier et al. 2017).

Bondi accretion also assumes that matter falling on to the neutron star accretes passively on to the neutron star. However, the gravitational potential energy released as matter accretes on to the neutron star is emitted in radiation and matter outflows that can significantly decrease the accretion rate below the Bondi rate. The Eddington limit is an extreme case of this radiative feedback that assumes all of the energy released is converted into radiation, and the momentum carried by this radiation exerts a force on the inflowing material. This radiation limits the amount of accretion on to an object. The radiative force at radius r is

$$F_{rad} = \frac{L_{rad}}{4\pi r^2} \frac{\sigma}{c}, \quad (4)$$

where L_{rad} is the radiative luminosity, σ is the cross-section, and c is the speed of light. Setting this force equal to the gravitational force ($F_{\text{grav}} = GM_{\text{NS}}m/r^2$, where m is the mass of the accreting particle), we derive the Eddington luminosity

$$L_{\text{Edd}} = 4\pi GM_{\text{NS}}/(\sigma c). \quad (5)$$

For accreting, fully ionized hydrogen, m is the proton mass and σ can be set to the Thompson cross-section. Although most studies use these assumptions to calculate the Eddington luminosity, for some scenarios, such as fallback accretion in supernova, the opacity per unit mass can be much higher (Fryer, Colgate & Pinto 1999a), lowering the Eddington accretion rate.

The Eddington limit on accretion assumes that the radiative luminosity is equal to the gravitational potential energy released:

$$\dot{M}_{\text{Edd}} = 4\pi mr_{\text{NS}}/(\sigma c), \quad (6)$$

where r_{NS} is the neutron star radius. This limit on the accretion rate assumes spherical symmetry, the radiation is not trapped in the flow and that all the accretion energy is released in radiation. For low accretion rates, many of these assumptions are valid. But as the accretion rate increases, these assumptions lose their validity.

Here we review each assumption individually. Determining whether the radiation is trapped in the flow is difficult without full calculations, but a first-order estimate can be made by comparing the diffusive transport velocity (v_{diff}):

$$v_{\text{diff}} = \lambda/Dc, \quad (7)$$

where D is the size of the transport region (some fraction of the stellar radius) to the infall velocity, typically set to the free-fall velocity (v_{ff}):

$$v_{\text{ff}} = \sqrt{2GM_{\text{enc}}/r}, \quad (8)$$

where M_{enc} is the enclosed mass of the star at radius r . Using these approximations, it is found that, except at the beginning of the CE phase when the neutron star is in the outer layers of the hydrogen envelope when $\dot{M} < 10^{-4} M_{\odot} \text{ yr}^{-1}$, the radiation is trapped in the flow (Chevalier 1993; Fryer et al. 1996). Recall that, for our nucleosynthesis models, we are only concerned with accretion rates above $1 M_{\odot} \text{ yr}^{-1}$ where the radiation is truly trapped in the flow ($v_{\text{diffusion}} \ll v_{\text{infall}}$) and the assumptions needed for the Eddington limit are not applicable.

What about the assumption that all of the energy is emitted in photons? If the radiation is trapped in the flow, the material will shock and settle on to the neutron star. By calculating the post-shock entropy of the material and assuming it piles on to the neutron star, we can derive the temperature and density properties of this accreted material. These estimates find that, unless the entropy is above $10,000 k_{\text{B}}$ per nucleon, the temperature and density conditions are such that most of the gravitational energy released will be converted into neutrinos and escape the star without impeding the inflow (Chevalier 1989; Fryer et al. 1996). In CE models, the entropy ranges between 10 and $100 k_{\text{B}}$ per nucleon and, to date, no one has constructed a way to avoid rapid neutrino cooling in CE scenarios. For CE systems, only a fraction of the energy is emitted in photons and this assumption of the Eddington approximation is also never satisfied. For systems where the CE phase ends up with the NS merging with its companion's helium core, neutrino emission increases dramatically, allowing the neutron star to incorporate material at the high Bondi rates predicted for these dense conditions. This merger ultimately forms a rapidly accreting black hole that may produce ultra-long gamma-ray bursts (Fryer & Woosley 1998).

Although it seems that Bondi–Hoyle accretion assumptions are most applicable to our problem, not all of the energy is converted to neutrinos and photons, some goes into kinetic energy that ejects a fraction of the accreting material (see Section 2.2). It is this ejecta that is the subject of our nucleosynthesis study. We will discuss this ejecta in more detail in Section 2.2, but it is important to understand that the ejecta may also alter the accretion. We will decrease the accretion rate in our Bondi–Hoyle solution to approximate this effect. In this project we use two bounds to match the range of efficiencies in simulations: $\lambda_{\text{BHL}} = 1/4, 1/40$. The lower value is set to try to capture both asymmetric accretion and ejecta affects that lower the accretion rate.

The accretion during the CE phase depends on the structure of the star which, in turn, depends upon both the stellar mass and evolutionary stage. To estimate the NS accretion rates in the CE phase, we use a coarse grid of stellar models computed using the MESA stellar evolution code (Paxton et al. 2011, 2013, 2015, 2018), ranging from 8 to 25 solar masses with initial metallicities in the range $10^{-4} \leq Z \leq 2 \times 10^{-2}$. The massive star models ($M_{\text{ini}} \geq 12 M_{\odot}$) are the ones from Ritter et al. (2018). The $8 M_{\odot}$ models were computed using the same input physics as in Jones et al. (2013). We refer the reader to those papers for a more thorough description of the stellar evolution calculations.

We study the structure of each of these models as the star evolves, focusing on periods of time when the star is expanding and a CE phase is likely to occur. Fig. 1 shows the radius evolution of our stars as a function of time with the points showing the specific times used in our study. As the neutron star spirals into the star, the accretion rate on to it increases. The corresponding accretion rates (assuming $\lambda_{\text{BHL}} = 1/4$) as a function of radius for the 12, 15, and $20 M_{\odot}$ stars at different evolutionary times is shown in Fig. 2. In the bulk of the envelope, the accretion rate lies between 1 and $10^5 M_{\odot} \text{ yr}^{-1}$ and we will focus on these rates, but if the neutron star spirals into the core, the accretion rate will be higher.

2.2 Ejection of accreted mass

The accreted material is explosively unstable and early calculations suggested that some of the infalling material would gain enough energy to be ejected (Fryer et al. 1996). Estimates of the convective time-scale using the Brunt–Väisälä frequency (see, for example, Cox, Vauclair & Zahn 1983; Fryer et al. 1996) suggest that the time-scale that the material spends near the proto-neutron star surface is milliseconds in duration. This initial study focused on CE accretion scenarios, but most of the subsequent, more systematic, multidimensional work focused on the higher accretion rates seen in supernova fallback (Fryer et al. 2006; Fryer 2009). Although these studies focused on accretion rates above $10^4 M_{\odot} \text{ yr}^{-1}$, they showed the same features as the CE models studied in Fryer et al. (1996). The accreted material falls down toward the proto-neutron star surface. A fraction of this material is heated and accelerated to above escape velocities, ejecting it from the system.

We designed a set of twelve trajectories based on these simulations, guided by the analytic models developed to understand these simulations. The accreting material accelerates nearly at free-fall until it falls within 10 km of the neutron star surface. The uncertainty in the flow lies in determining how quickly the flow is reversed and material is ejected. We study two extremes: a bounce scenario where the reverse is instantaneous, a convective scenario where the acceleration time-scale is on par with the convective turnover time-scale. For the latter, convective time-scale, we can estimate the acceleration time-scale from the Brunt = Väisälä frequency

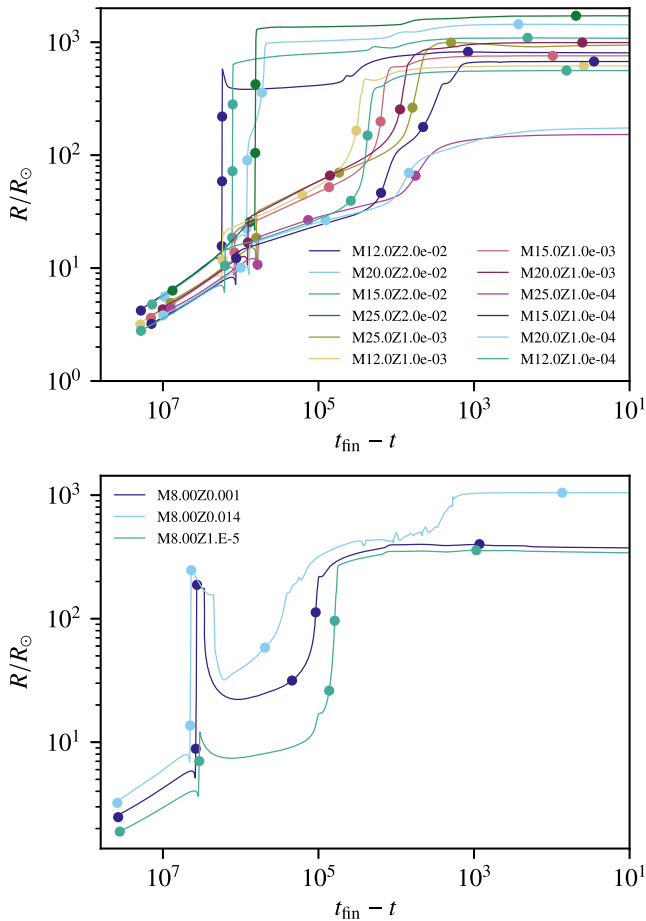


Figure 1. Radius evolution of the stellar models used in this study. The x -axis is time remaining until core collapse (or, in the case of some of the $8 M_{\odot}$ models, envelope ejection). The points indicate at which times stellar structures were used from the models in order to calculate the accretion rates.

($t_{\text{acceleration}} = 1/\omega_{\text{BV}}$) where

$$\omega_{\text{BV}}^2 = g/\rho(\partial\rho/\partial S)_P(\partial S/\partial r), \quad (9)$$

where ρ and S are the density and entropy, respectively (Cox, Vauclair & Zahn 1983). For conditions in supernovae and fallback this time-scale is on the range of 2 ms (Fryer & Young 2007). This time-scale estimates the growth time-scale of Rayleigh–Taylor instabilities, but this provides an approximate time-scale for the acceleration time-scale to reverse the shock. Fallback simulations suggest that the true answer lies between these two extremes.

We model these two extremes by two parametrized simulations: bounce and convective trajectories. The bounce trajectory assumes that material falls in adiabatically at free-fall until it reaches 20 km (10 km from the surface) and where it is assumed that the material bounce and is ejected at the escape velocity. For the convective trajectory, we assume that the material falls in at free-fall until it reaches a depth of 50 km, where we turn on a force that is strong enough to turn around the trajectory within the roughly 2 ms convective time-scale.

The temperature evolution of these two paradigms is shown in Fig. 3. The corresponding density evolution is shown in Fig. 4. In the bounce trajectory, in our first model, sharp increase of the temperature evolution profile (Fig. 3) mimics a hard stop for the infalling material prior to this expulsion. In our the convective model, the acceleration begins sooner but is more gradual.

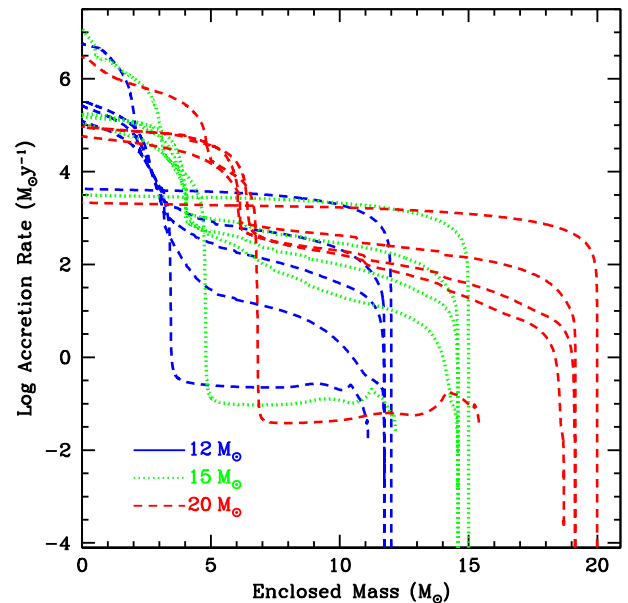


Figure 2. Accretion rate for a $1.4 M_{\odot}$ neutron star as a function of the position of the neutron star within the mass coordinate of its companion for the 12, 15, and $20 M_{\odot}$, solar metallicity stars for a range of times. At early times, the envelope is compact and the accretion rate is higher. As the star expands, the accretion rate in the envelope decreases. In the bulk of the envelope, the accretion rate lies between 1 and $10^4 M_{\odot} \text{ yr}^{-1}$. Here we assume $\lambda_{\text{BHL}} = 1/4$. The accretion rates may be an order of magnitude lower.

Although we expect some gain in entropy during the heating phase, we assume constant entropy evolution for our models. If we increase the entropy, we increase the temperature, and more heavy elements will be produced. Likewise, if we make the evolution even more gradual, the material will remain in a region of high nuclear burning longer, also producing more heavy elements. But our simulation-guided (Fryer et al. 1996, 2006; Fryer 2009) toy models will provide a gauge of the importance of this ejecta in GCE.

Typically ~ 10 – 25 per cent of the accreted material is ejected along the angular momentum axis (Fryer et al. 2006). It is this material that is the focus of our nucleosynthetic studies. In this paper, we focus on accretion rates between 1 and $10^5 M_{\odot} \text{ yr}^{-1}$. The rate rarely exceeds our highest accretion rate in common envelop situations and lower rates (occurring in initial phases of the CE) do not produce much nuclear burning. The inner infall, nuclear burning and ejection phases are so rapid (< 1 s) that we can assume the accretion rate is constant over any cycle.

Table 1 lists the trajectories investigated in this paper, and shown in Fig. 3. The trajectories labelled with ‘.C.’ are representative of the first model described above, while those labelled with ‘.D.’ are representative of the second delayed model.

3 NUCLEOSYNTHESIS CALCULATIONS FROM NEUTRON STAR ACCRETION

In this section we present the nucleosynthesis yields of the trajectories described in Section 2.2 and listed in Table 1. The composition of the accreted material has a scaled solar isotopic distribution (Asplund et al. 2009), with metallicity $Z_m = 0.02$.

The nuclear network includes 5234 isotopes and 74 313 reactions from the different nuclear physics compilations and rates available (see e.g. Pignatari et al. 2016). The $3\text{-}\alpha$ and $^{12}\text{C}(\alpha, \gamma)^{16}\text{O}$ by

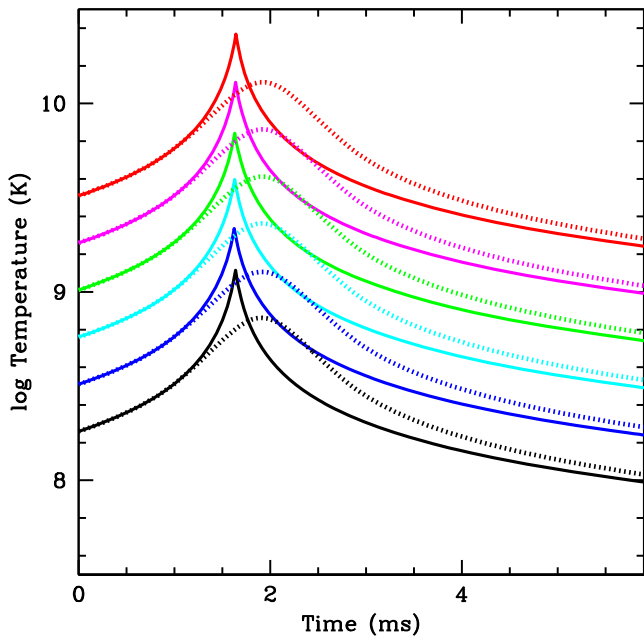


Figure 3. Temperature as a function of time for our trajectories at different accretion rates: $1 M_{\odot} \text{ yr}^{-1}$ (black lines), $10 M_{\odot} \text{ yr}^{-1}$ (blue lines), $10^2 M_{\odot} \text{ yr}^{-1}$ (cyan lines), $10^3 M_{\odot} \text{ yr}^{-1}$ (green lines), $10^4 M_{\odot} \text{ yr}^{-1}$ (magenta lines), and $10^5 M_{\odot} \text{ yr}^{-1}$ (red lines). Solid lines refer to our model mimicking a hard stop of the infalling material, dotted lines correspond to a more gradual turn-around of the ejecta (both described in Section 2.2).

Fynbo et al. (2005) and Kunz et al. (2002) respectively, and the $^{14}\text{N}(p,\gamma)^{15}\text{O}$ by Imbriani et al. (2005). The reaction rate $^{13}\text{C}(\alpha,n)^{16}\text{O}$ is taken from Heil et al. (2008), and the $^{22}\text{Ne}(\alpha,n)^{25}\text{Mg}$ and $^{22}\text{Ne}(\alpha,\gamma)^{26}\text{Mg}$ rates are from Jaeger et al. (2001) and Angulo et al. (1999). Experimental neutron capture reaction rates are taken when available from the KADoNIS compilation (Dillmann et al. 2006). For neutron capture rates not included in KADoNIS, we refer to the JINA REACLIB database, V1.1 (Cyburt 2011). The weak rates for light and intermediate-mass species are provided by Oda et al. (1994) or Fuller, Fowler & Newman (1985), by Langanke & Martínez-Pinedo (2000) for mass number $45 < A < 65$ and for the weak interaction between protons and neutrons. Finally, for heavy species with $A > 65$ we use Goriely (1999).

Besides the $^{14}\text{N}(p,\gamma)^{15}\text{O}$ mentioned above, proton capture rates have different sources like the NACRE compilation (Angulo et al. 1999) and Iliadis et al. (2001) for isotopes in the mass region between ^{20}Ne and ^{40}Ca . Proton captures on isotopes heavier than ^{40}Ca are given by the JINA REACLIB database. The $^{13}\text{N}(p,\gamma)^{14}\text{O}$ rate is taken from Caughlan & Fowler (1988), and proton captures on ^{27}Al from Champagne & Wiescher (1992).

For our simulations we have used material accreted with solar composition. This approximation does not affect conclusions in this paper. Indeed, at the lower accretion rates seed nuclei might have large effects on the distribution of products, but their impact on the final yields is marginal. On the other hand, at the higher accretion rates investigated in this paper the material accreted enters in nuclear statistical equilibrium (NSE) at extreme conditions (Table 1), so that the final yields are largely insensitive to the initial isotopic distribution (and to the electron fraction Y_e). As we will see in the following sections, nucleosynthesis in these trajectories is dominating the total integrated ejecta for GCE.

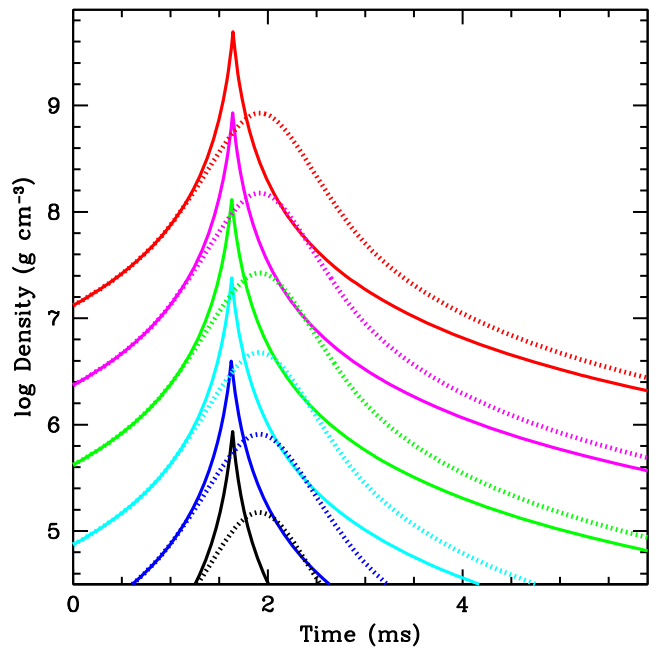


Figure 4. Density as a function of time for our trajectories at different accretion rates: $1 M_{\odot} \text{ yr}^{-1}$ (black lines), $10 M_{\odot} \text{ yr}^{-1}$ (blue lines), $10^2 M_{\odot} \text{ yr}^{-1}$ (cyan lines), $10^3 M_{\odot} \text{ yr}^{-1}$ (green lines), $10^4 M_{\odot} \text{ yr}^{-1}$ (magenta lines), and $10^5 M_{\odot} \text{ yr}^{-1}$ (red lines). Solid lines refer to our model mimicking a hard stop of the infalling material, and dotted lines correspond to a more gradual turn-around of the ejecta (both described in Section 2.2).

3.1 Yields at differing accretion rates

Production of isotopes at various accretion rates on to the surface of the compact object was investigated. Accretion rates varied from $1 M_{\odot} \text{ yr}^{-1}$, where the neutron star first comes into contact with the companion, to the maximum accretion rate of $10^5 M_{\odot} \text{ yr}^{-1}$, corresponding to the final stages of accretion in the system when the neutron star reaches the helium core.

Tables 2 and 3 summarize the results of this section and give a list of the isotopes with the highest overproduction, the increase in the abundance of an isotope relative to its initial abundance in the accreted material, at the accretion rates 10^4 and $10^5 M_{\odot} \text{ yr}^{-1}$ for the trajectories investigated. Trajectories at lower accretion rates do not show the same extent of overproduction, and therefore contribute minimally to our GCE results. Table 4 shows the top five isotopes overproduced in each of the trajectories investigated. Those isotopes most produced in these trajectories are also given in the relevant sections. In Tables A1 and A2 the isotopic yields of stable isotopes (with contributions from decayed unstable isotopes) are provided for the trajectories listed in Table 1. Complete radiogenic contribution is considered for these abundances. Undecayed abundances are also provided in separate tables available online at CANFAR. The corresponding overproduction factors are given in Tables A3 and A4.

Complete isotopic production factors and elemental abundances are shown in Figs 5 and 6, respectively, where results from the two sets of trajectories at accretion rates can be compared (see discussion here below). Fig. 7 shows the integrated fluxes for each of the Mod.C accretion rates. Figs 8 and 9 show the final isotopic production factors, zoomed in the mass region $40 \lesssim A \lesssim 100$, and the electron fraction Y_e obtained. Our results show that the largest contributions to GCE must come from those trajectories at higher accretion

Table 1. List of trajectories investigated in this paper, along with peak temperatures in those trajectories. The first column includes those trajectories in Fig. 3 which have undergone a sudden change in direction during the accretion, while those with a more gradual turnaround are listed in the third column. The accretion rates range from 1 to $10^5 M_{\odot} \text{yr}^{-1}$ as detailed in Section 2. Temperatures have been clipped in these models at 10 GK, as reaction rates tables above this threshold are not available.

Trajectory name	Peak T_9C	Trajectory name	Peak T_9D	Accretion rate ($M_{\odot} \text{yr}^{-1}$)
mod.C.ar1d0	1.303	mod.D.ar1d0	0.728	1
mod.C.ar1d1	2.166	mod.D.ar1d1	1.278	10
mod.C.ar1d2	3.981	mod.D.ar1d2	2.306	10^2
mod.C.ar1d3	6.952	mod.D.ar1d3	4.090	10^3
mod.C.ar1d4	10.00	mod.D.ar1d4	7.286	10^4
mod.C.ar1d5	10.00	mod.D.ar1d5	10.00	10^5

Table 2. Table showing those isotopes overproduced in the given ranges for each of the accretion rates shown in the mod.C trajectories.

Overproduction $x_{\text{fin}}/x_{\text{ini}}$	$10^4 M_{\odot} \text{yr}^{-1}$	$10^5 M_{\odot} \text{yr}^{-1}$
$10^4 < x < 10^5$	$^{76, 77}\text{Se}$, $^{60, 61}\text{Ni}$, $^{72, 73}\text{Ge}$, $^{86, 87}\text{Sr}$, ^{75}As , ^{82}Kr , $^{69, 71}\text{Ga}$, $^{63, 65}\text{Cu}$, ^{96}Ru , ^{89}Y , $^{66, 67, 68}\text{Zn}$, ^{94}Mo ,	^{84}Kr , $^{67, 68, 70}\text{Zn}$, $^{63, 65}\text{Cu}$, ^{89}Y , ^{58}Fe , ^{86}Kr ,
$10^5 < x < 10^6$	^{70}Ge , ^{64}Zn , ^{80}Kr , ^{93}Nb ,	^{88}Sr , ^{87}Rb , $^{62, 64}\text{Ni}$
$10^6 < x < 10^7$	^{74}Se , ^{78}Kr , ^{84}Sr , $^{90, 91}\text{Zr}$	–
$10^7 < x$	^{92}Mo	–

Table 3. Table showing those isotopes overproduced in the given ranges for each of the accretion rates shown in the mod.D trajectories.

Overproduction $x_{\text{fin}}/x_{\text{ini}}$	$10^4 M_{\odot} \text{yr}^{-1}$	$10^5 M_{\odot} \text{yr}^{-1}$
$10^4 < x < 10^5$	$^{58, 61}\text{Ni}$	^{76}Ge , ^{50}Ti , $^{61, 62}\text{Ni}$, $^{63, 65}\text{Cu}$, ^{82}Se , $^{66, 67, 68, 70}\text{Zn}$, ^{58}Fe ,
$10^5 < x < 10^6$	–	^{88}Sr , ^{87}Rb , ^{64}Ni , ^{86}Kr , ^{54}Cr

Table 4. Five most overproduced isotopes for each of the accretion rates investigated.

Model	Most overproduced isotope
mod.C.ar1d0	^{42}Ca , ^{21}Ne , ^{74}Se , ^{18}O , ^7Li
mod.C.ar1d1	^{32}Ba , ^{80}Ta , ^{98}Ru , ^{31}P , ^{38}La
mod.C.ar1d2	^{58}Ni , ^{98}Ru , ^{62}Ni , ^{51}V , ^{61}Ni
mod.C.ar1d3	^{64}Zn , ^{51}V , ^{58}Ni , ^{62}Ni , ^{61}Ni
mod.C.ar1d4	^{91}Zr , ^{90}Zr , ^{78}Kr , ^{74}Se , ^{92}Mo
mod.C.ar1d5	^{86}Kr , ^{62}Ni , ^{64}Ni , ^{87}Rb , ^{88}Sr ,
mod.D.ar1d0	^{31}P , ^{33}S , ^{15}N , ^{18}O , ^7Li
mod.D.ar1d1	^{23}Na , ^{33}S , ^{42}Ca , ^{21}Ne , ^7Li
mod.D.ar1d2	^{36}Ce , ^{41}K , ^{44}Ca , ^{43}Ca , ^{42}Ca
mod.D.ar1d3	^{64}Zn , ^{51}V , ^{58}Ni , ^{61}Ni , ^{62}Ni
mod.D.ar1d4	^{64}Zn , ^{60}Ni , ^{62}Ni , ^{58}Ni , ^{61}Ni
mod.D.ar1d5	^{54}Cr , ^{88}Sr , ^{86}Kr , ^{87}Rb , ^{64}Ni

Table 5. Population synthesis calculations.

Metallicity	CE systems
0.02	7172
0.002	12234
0.0002	7172

rates. In these conditions, hydrogen is fully burned allowing high abundance overproductions at the iron group and beyond. Lower accretion rates contribute marginally to the enrichment of ejected material, both because the material is incompletely burnt and the amount of material ejected is much smaller. Proton-rich material is highly overproduced in trajectory mod.C.ar1d4, and this is the source of most of the proton-rich material ejected from the system. This trajectory reaches high enough temperatures that the accreted fuel burns efficiently, with a low enough peak density such that electron captures do not become dominant causing a shift in the Y_e and peak production to more neutron-rich isotopes.

3.1.1 Accretion rate $1 M_{\odot} \text{yr}^{-1}$: mod.C.ar1d0 and mod.D.ar1d0

The dominant reactions are proton captures from the H-rich accreted material, followed by β^+ decays bringing the material back towards the valley of stability in the mod.C.ar1d0 case. Some (p, α) reactions are evident in this region, hindering the flow of material to heavier masses.

Significant increases in the abundance of ^7Li can be seen for both mod.C.ar1d0 and mod.D.ar1d0 (top left panel of Fig. 5) with both trajectories showing overproduction factors of $\sim 10^6$. This occurs due to efficient ^3He (α , γ) ^7Be , followed by β^+ decays. ^{15}N and ^{18}O are also increased significantly, by factors of about 150 and 250 for mod.C.ar1d0, and 280 and 510 for the delayed trajectory. Enhancements of light and intermediate-mass elements are comparable for the two trajectories, until the mass region $A \sim 50$. Beyond this mass, the delayed trajectory does not show efficient production for the heavier elements, while in mod.C.ar1d0 final abundances are enhanced up to $A \sim 80$. This is due to the higher peak temperature reached compared to the mod.D.ar1d0 model (1.303 GK compared to 0.728 GK), causing a build-up of heavier nuclei mostly via proton capture reactions.

Panel a of Fig. 6 shows that neither of the trajectories at this accretion rate allows any burning of material above $Z = 40$. The conditions at this accretion rate are not extreme enough to allow proton captures on these heavier nuclei, or to cause photodisintegration on the heavier elements present in the accreted material.

^{74}Se , ^{78}Kr , and ^{84}Sr (the lightest of the p-nuclei) all have overproduction factors greater than 10^2 for mod.C.ar1d0 at this accretion rate, whereas the delayed trajectory shows no production of these isotopes. Inspection of flux charts for mod.C.ar1d0 shows a proton capture path with β^+ decays in the proton-rich side of the valley of stability, like for the rp-process (Schatz et al. 2001). This becomes most evident above the $N = 20$ neutron magic number [see panel (a) of Fig. 7]. As can be seen from the first columns of Tables A1 and A4, the H fuel accreted from the companion star

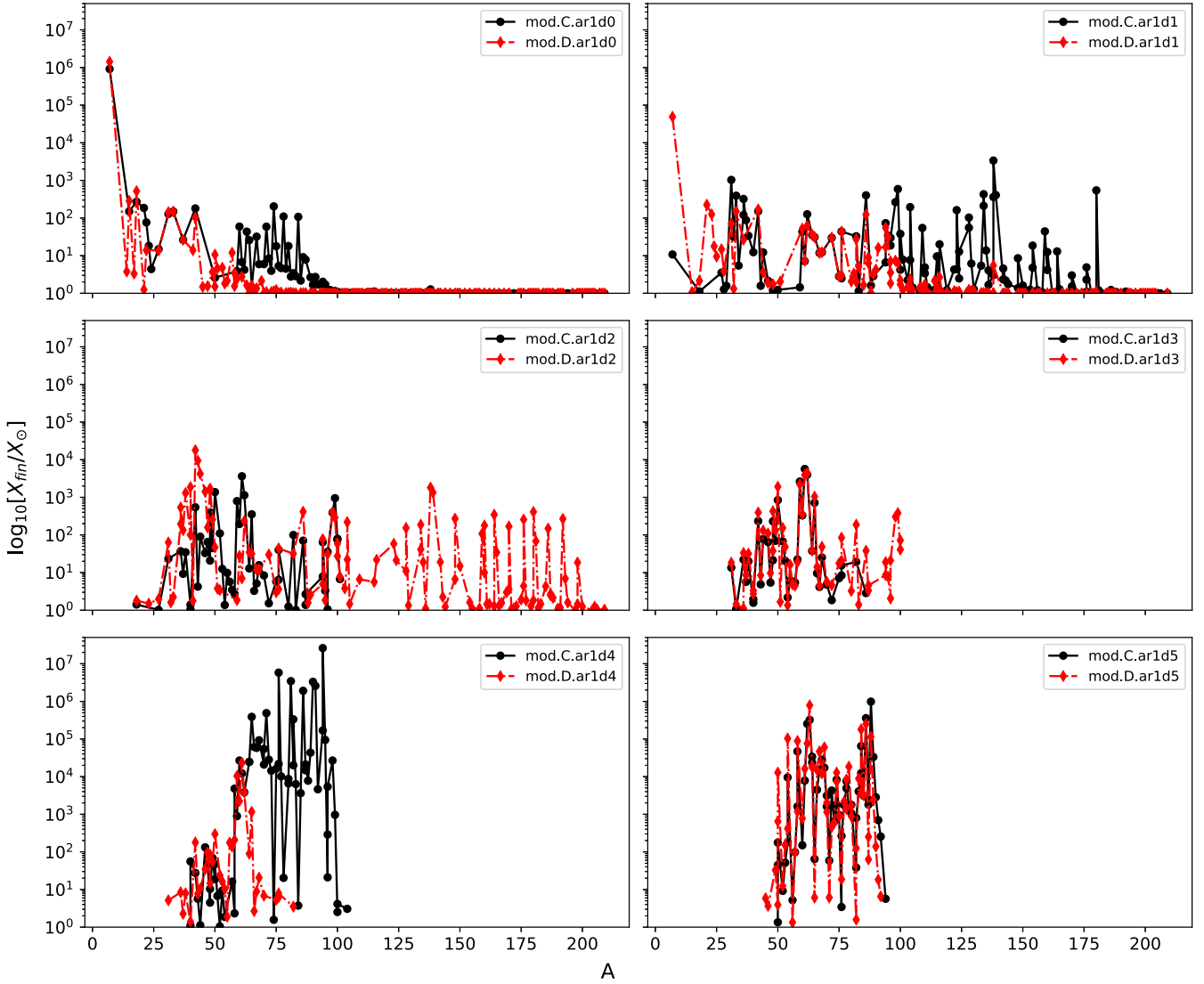


Figure 5. Overproduction factors for trajectories listed in Table 1 are shown. Abundances for delayed trajectories (‘mod.D.’) are shown in red, and in black for ‘mod.C.’ trajectories. Relative accretion rates are indicated in each panel.

remains largely unburnt under these conditions – only 0.2 per cent of the initial abundance of H is burnt for both of these trajectories.

3.1.2 Accretion rate $10 M_{\odot} \text{yr}^{-1}$: *mod.C.ar1d1* and *mod.D.ar1d1*

Nucleosynthesis in *mod.C.ar1d1* results in overproduction of a large number of isotopes up to $A \sim 157$, due to the higher peak temperatures experienced in this trajectory as compared with the *mod.C.ar1d0* case, allowing for more efficient proton captures in the accreted material, whilst remaining below the threshold for activation of photodisintegration of heavier material seen in higher accretion rate models. The highest mass isotope to be overproduced under these conditions is ^{180}Ta (with a production factor of 5.4×10^2), and the isotopes with the greatest overproduction are ^{138}La and ^{31}P (3.3×10^3 and 1.0×10^3 times initial abundance, respectively). Fourteen other isotopes – ^{33}S , $^{35,37}\text{Cl}$, ^{42}Ca , ^{62}Ni , ^{84}Sr , $^{96,98}\text{Ru}$, ^{102}Pd , ^{120}Te , ^{126}Xe , $^{130,132}\text{Ba}$, and $^{136,138}\text{Ce}$ all have production factors of between 10^2 and 10^3 .

In *mod.D.ar1d1* abundances are greatest at lower masses. ^7Li , ^{21}Ne , ^{23}Na , ^{33}S , ^{42}Ca , and ^{84}Sr have overproduction factors of be-

tween 10^2 and 10^3 . The much reduced range of highly overproduced isotopes is again due to the lower temperatures experienced by the delayed trajectory on in-fall of the material. The peak temperature of *mod.D.ar1d1* is similar to the peak temperature of *mod.C.ar1d0* trajectory discussed before (see Table 1). Differences in the two abundance distributions are due to the temperature histories of the two trajectories, with the delayed trajectory exposed for longer to more extreme conditions.

Production factors and abundances are shown in the top right panels of Figs 5 and 6, respectively. The mass fraction of the majority of stable isotopes above $Z = 40$ remains unchanged, as was the case for the previous section. Peak temperatures from our simulations do not increase beyond ≈ 2 GK (Fig. 3) and burning occurs on a time-scale of order milliseconds. Neither α nor proton captures have high enough probability at these temperatures to trigger complete burning of the accreted material.

Flux nucleosynthesis plots for this accretion rate are similar to those for the $1 M_{\odot} \text{yr}^{-1}$ case, and are shown in panel (b) of Fig. 7.

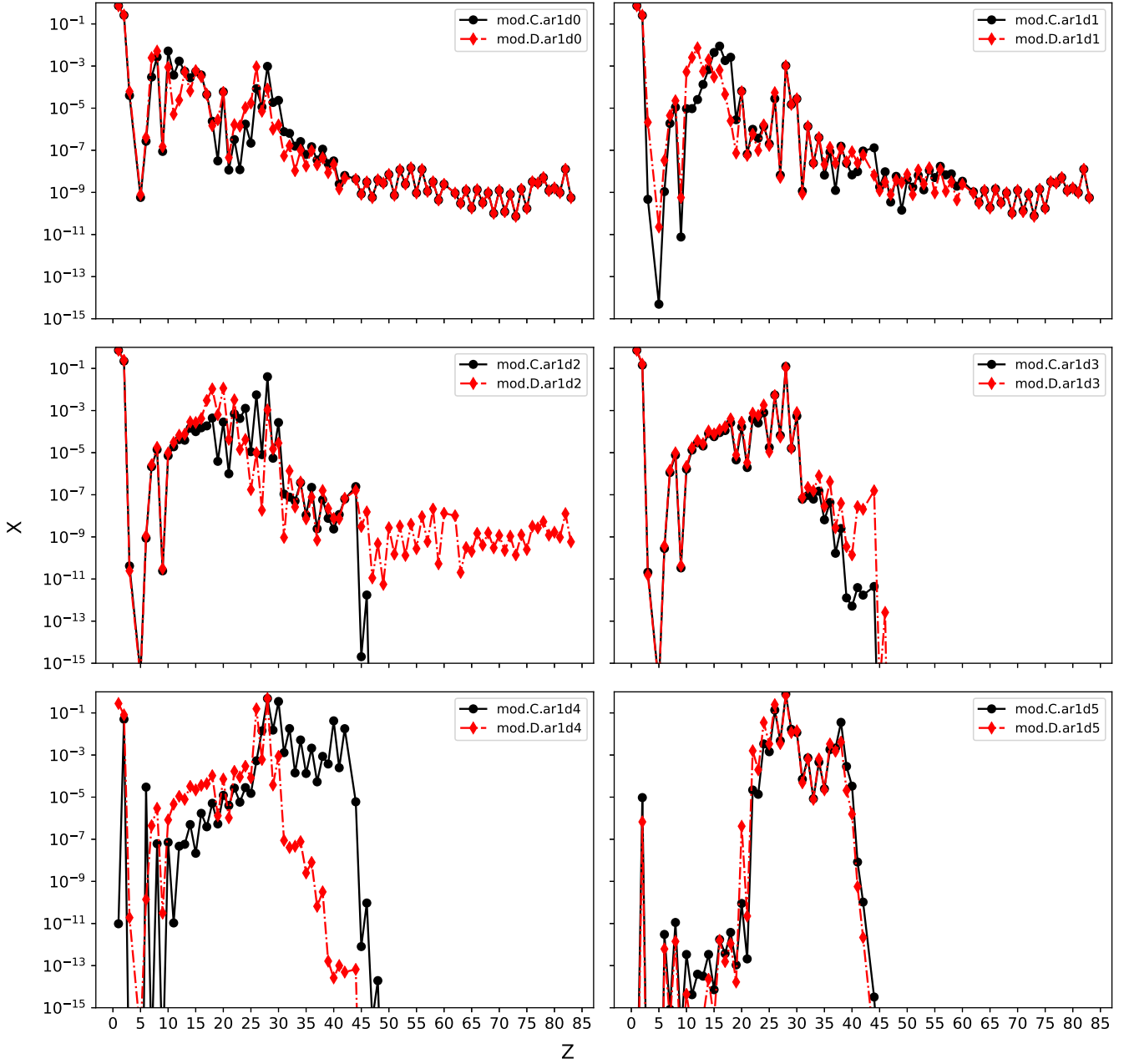


Figure 6. Element abundance distributions in mass fraction with respect to atomic number are shown for the same cases in Fig. 5. Contribution from radioactive decay is considered. Abundances for delayed trajectories (‘mod.D.’) are shown in red, and black for ‘mod.C.’ trajectories. Most of the element abundances in the first two panels remain unchanged from their initial distributions, while significant changes can be observed at higher accretion rates.

3.1.3 Accretion rate $10^2 M_{\odot} \text{yr}^{-1}$: *mod.C.ar1d2* and *mod.D.ar1d2*

Abundance production for *mod.C.ar1d2* is clustered at mass between $A \sim 25$ and 100. ^{51}V and $^{61,62}\text{Ni}$ are overproduced by factors larger than 10^3 . Eight other isotopes have production factors greater than 10^2 : ^{42}Ca , ^{48}Ti , ^{52}Cr , $^{58,60}\text{Ni}$, ^{64}Zn , and $^{96,98}\text{Ru}$. The flux nucleosynthesis plot [panel (c) of Fig. 7] for this trajectory shows a relevant difference compared to lower accretion rates. Burning proceeds further from the valley of stability, due to the more efficient proton captures at high temperatures. The α -captures on intermediate-mass isotopes are activated. Heavier isotopes are destroyed by (γ, n) photodisintegration reactions, and a mild flux

of (n, γ) reactions is also activated. As for lower accretion rates, a large proportion of the infalling material is not burnt (Table A1) with only ≈ 0.3 per cent of the hydrogen fuel being consumed. The peak temperatures in this trajectory is 3.981 GK.

The delayed trajectory *mod.D.ar1d2* shows an abundance distribution extremely different from *mod.C.ar1d2*. Production extends to higher mass isotopes due to the longer time that the material spends at high temperature, and without yet relevant activation of photodisintegration reactions. There are 22 isotopes enhanced by a factor between 10^2 and 10^3 , and among them 8 have masses above $A = 150$. ^{38}Ar , ^{41}K , $^{43,44}\text{Ca}$, ^{45}Sc , $^{47,48}\text{Ti}$, and $^{136,138}\text{Ce}$ show overabundances between 10^3 and 10^4 , and ^{42}Ca greater than 10^4 .

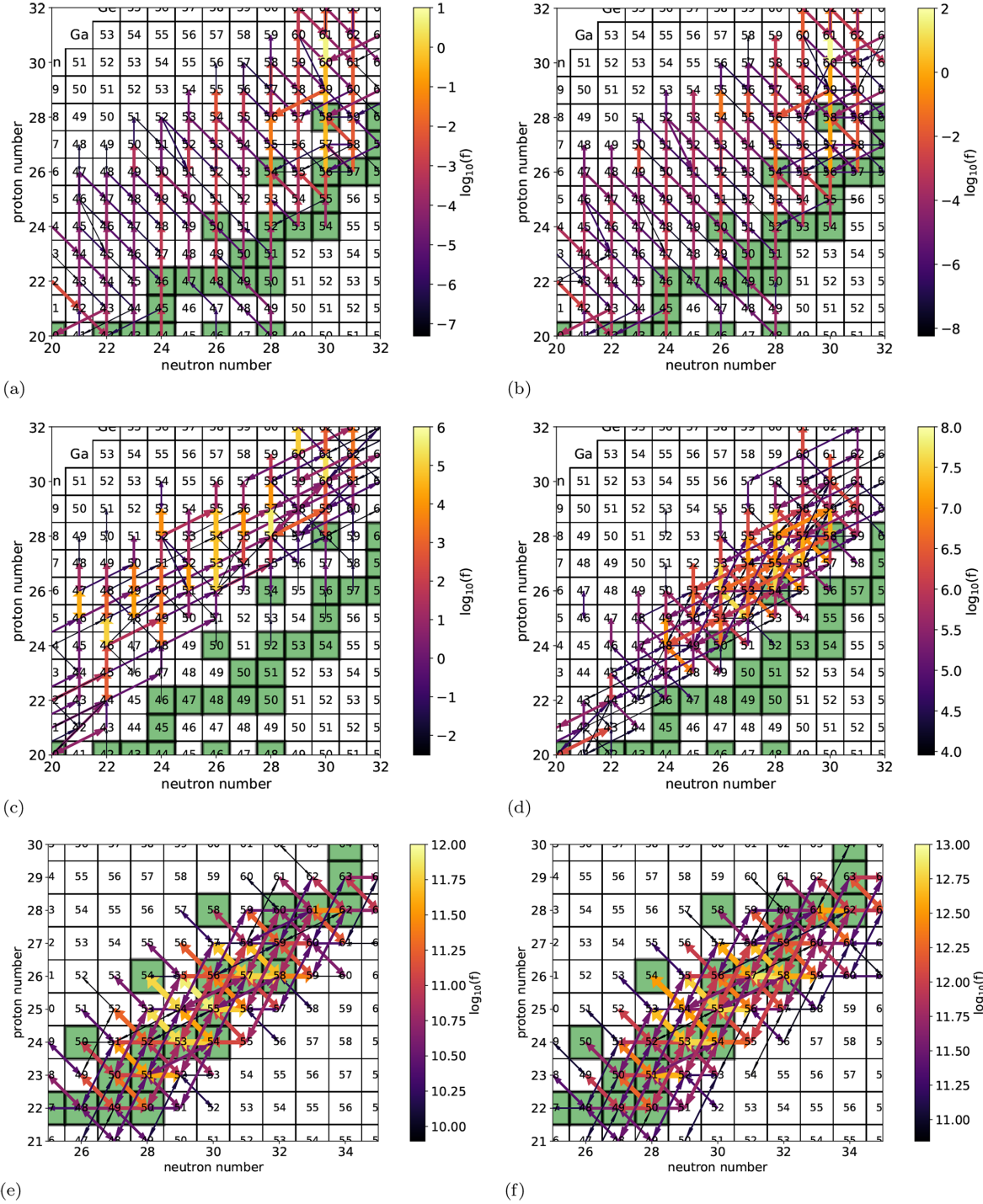


Figure 7. Figure showing the distribution of fluxes ($\delta X / \delta t$) for each reaction (units s^{-1}) for the mod.C trajectories, normalized to the maximum flux in each of those trajectories. Top left to bottom, these correspond to the different accretion rates investigated in this paper for the mod.C case, lowest accretion rate to highest.

Temperatures are not high enough to initiate the photodisintegration reactions observed in mod.C.ar1d2.

It can be seen from the middle left panel of Fig. 6 that there is a significant change in the mass fraction of elements with $50 < Z < 65$, although the very heaviest elements (with $Z > 65$) which are investigated in this work remain largely unchanged in their abundances. The distributions of both of the C and D

models are identical in the upper panels of Fig. 6, implying that the distribution cannot be changed from the initial abundances. This is verified by comparison with Fig. 5, where the production factors for all isotopes above $A = 150$ and most above $A = 100$ are negligible. Some elements with $50 > Z > 65$ have abundances increased by up to 3 orders of magnitude. However, because of their small intrinsic abundances and the small contribution to

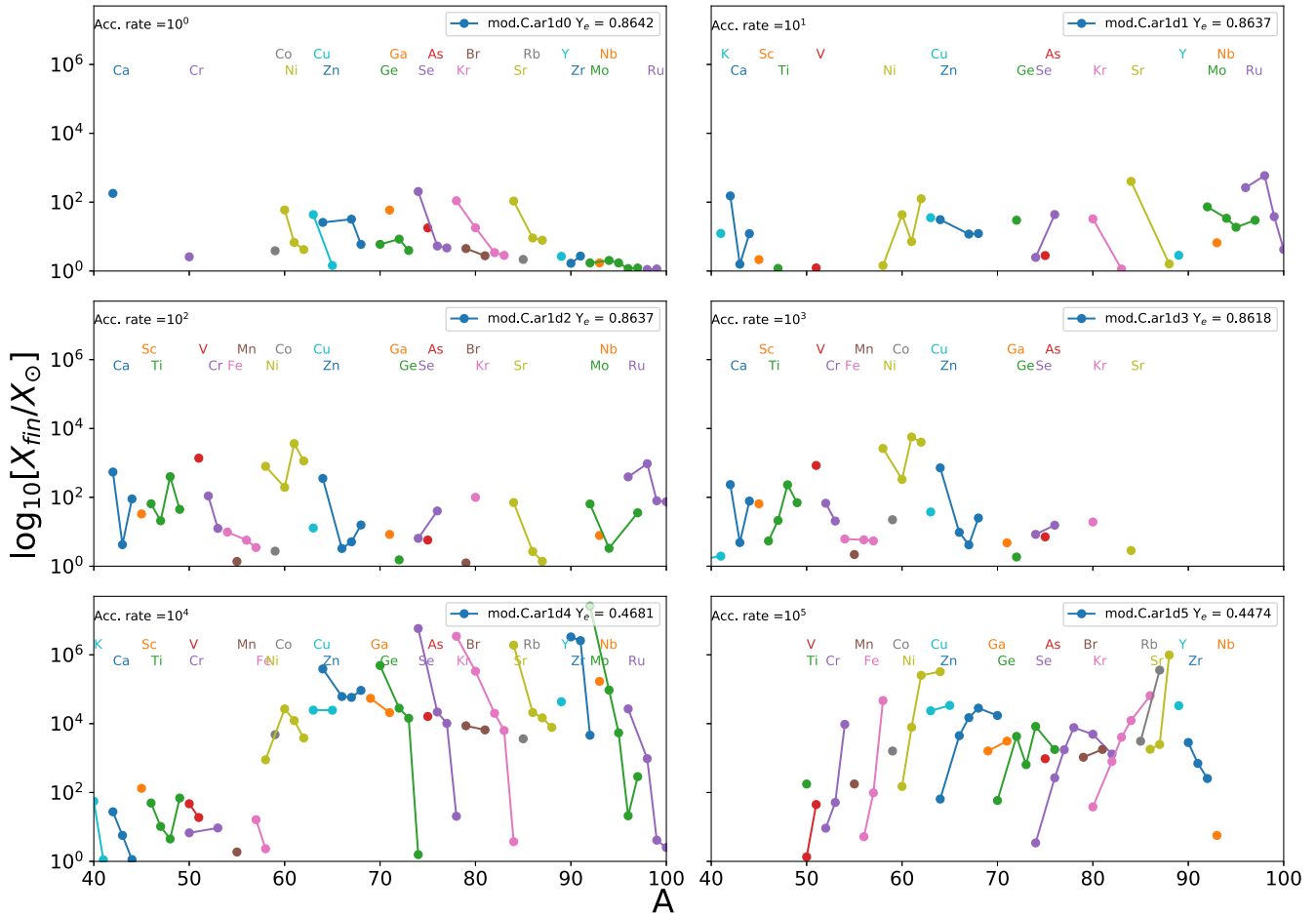


Figure 8. The isotopic distribution between $A = 40$ and 100 is shown for trajectories ‘mod.C.’ at different accretion rates.

the final integrated ejecta, this effect is not important to GCE models.

3.1.4 Accretion rate $10^3 M_{\odot} \text{yr}^{-1}$: mod.C.ar1d3 and mod.D.ar1d3

Material at this accretion rate reaches a peak temperature of 6.952 GK in the mod.C.ar1d3 trajectory and 4.090 GK in the mod.D.ar1d3 case, although for both trajectories the accreted material remains largely unburnt. The trajectory mod.C.ar1d3 reaches NSE, and the destruction of heavier elements by photodisintegration as already seen for mod.C.ar1d2 now occurs in both trajectories. Isotopes are produced most efficiently in the mass region $50 \lesssim A \lesssim 100$, including species in the iron-group region and up to Ru. For both trajectories, a significant increase of greater than 10^3 in the abundances of $^{58, 61, 62}\text{Ni}$ is seen. In mod.C.ar1d3 overabundances greater than 10^2 are obtained for 5 other isotopes: ^{48}Ti , ^{42}Ca , ^{60}Ni , ^{64}Zn and ^{51}V , and 9 in the delayed trajectory mod.D.ar1d3: ^{45}Sc , $^{42, 44}\text{Ca}$, $^{48, 49}\text{Ti}$, ^{52}Cr , ^{60}Ni , ^{80}Kr , and ^{96}Ru . Elemental distributions of the two trajectories for this accretion rate are similar (middle left panel of Fig. 6) up to $Z = 30$, however there are significant differences in the abundances of Mo, Nb, and Ru, none of which are overproduced in mod.C.ar1d3, and for some isotopes of Kr and Sr where a difference in overproduction factors of over an order of magnitude can be observed.

In panel (d) of Fig. 7, the integrated reaction flows are shown for mod.C.ar1d3. In these conditions, α captures and β decays are now

the dominant reaction pathways. Proton captures are still active, but they do not push material from the line of stability as efficiently as in panel (c) of Fig. 7. Approximately 50 per cent of the initial abundance of He is burnt in this trajectory.

3.1.5 Accretion rate $10^4 M_{\odot} \text{yr}^{-1}$: mod.C.ar1d4 and mod.D.ar1d4

Among the trajectories described in this section, mod.C.ar1d4 is the first case to undergo complete burning of hydrogen, with this trajectory entering NSE). Significant overproduction for a large number of isotopes is observed: ^{74}Se , ^{78}Kr , ^{84}Sr , and $^{90, 91}\text{Zr}$ have final abundances over 6 orders of magnitude higher than initial, ^{92}Mo is overproduced by a factor of 2.6×10^7 . Excepting the Zr isotopes, all of these nuclei are classically defined as products of the p-process (Arnould & Goriely 2003; Rauscher et al. 2013; Pignatari et al. 2016). While these are proton-rich isotopes, for mod.C.ar1d4 we obtain a final neutron-rich distribution ($Y_e = 0.46$, Table A1). This is mostly due to the neutron-rich abundance signature in the Ni region, with 58 per cent of mass fraction as ^{62}Ni and only a minor contribution to ^{58}Ni . The zoomed isotopic distribution is shown in Fig. 8, bottom left panel. The abundance pattern of heavy isotopes is similar to neutrino-driven winds ejecta with proton-rich composition (e.g. Fröhlich et al. 2006; Roberts, Woosley & Hoffman 2010; Arcones & Montes 2011).

Partial burning of the hydrogen is observed for the delayed trajectory mod.D.ar1d4. Production for heavy isotopes is marginal

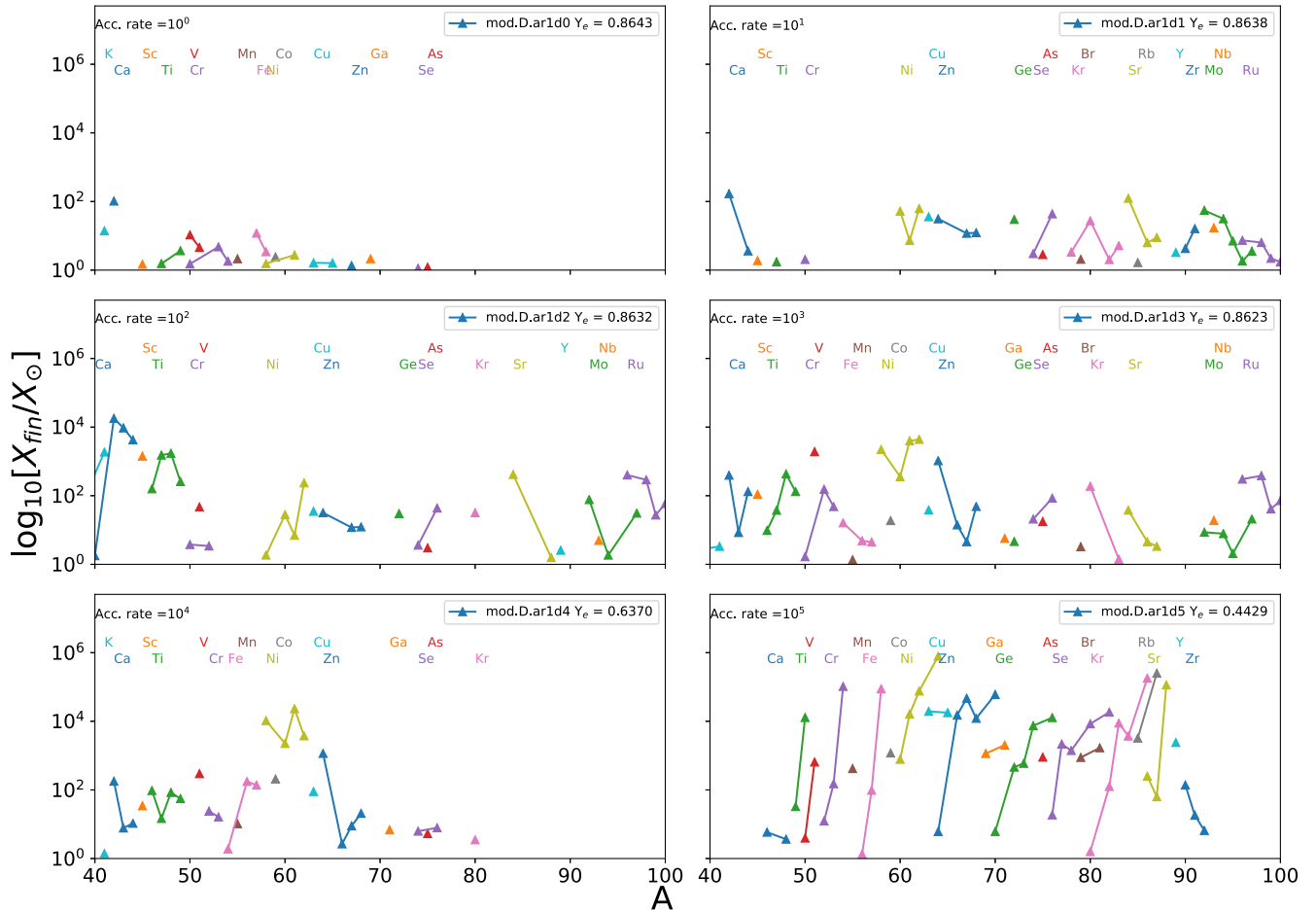


Figure 9. As for Fig. 8 but for delayed trajectories ('mod.D.').

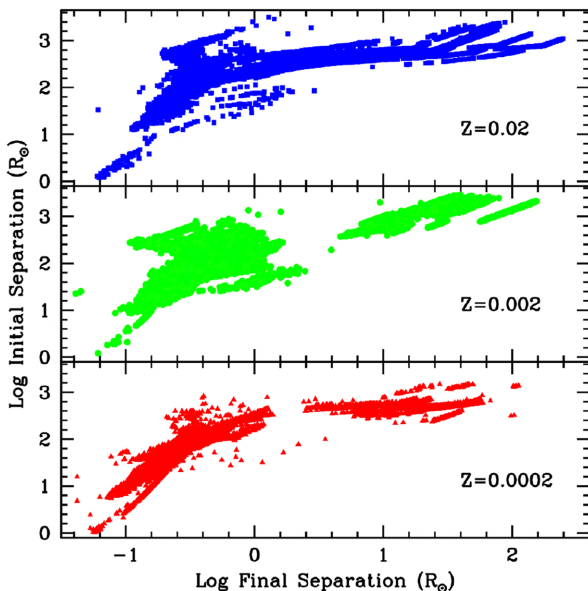


Figure 10. Initial versus final separation for all the binary systems undergoing a CE phase from our population synthesis simulations, given at three metallicities.

compared to mod.C.ar1d4 (Fig. 5), while intermediate-mass elements are made more efficiently (Fig. 6). Isotopes $^{58,61}\text{Ni}$ both have overproduction factors greater than 10^4 . As also shown in the bottom left panel of Fig. 9, p-process isotopes are not made in mod.D.ar1d4, with no significant production above $A \sim 80$. As we have seen for trajectories in the previous section, material above this mass has been destroyed by photodisintegration. Panel (e) of Fig. 7 shows the flux plot for mod.C.ar1d4. The material is in NSE, with the large amount of hydrogen allowing proton captures to occur and extending the abundance distribution to the proton-rich side of the line of stability. The lower densities reached in this model as compared with the mod.C.ar1d5 trajectory ensure that electron capture reactions are not favourable enough to reduce the Y_e .

The trajectory is in NSE with large fluxes in the iron group region, lower average and lower peak densities in this model lead to a more proton-rich distribution of products than the mod.C.ar1d5 case (see panel f of Fig. 7 for comparison). The flux plot is dominated by the reactions in NSE equilibrium around the iron group region during the NSE phase. In these simulations, the temperature and density freezeout is extremely fast and do not allow to significantly modify the integrated fluxes after the trajectories exit from NSE.

3.1.6 Accretion rate $10^5 M_{\odot}\text{yr}^{-1}$: mod.C.ar1d5 and mod.D.ar1d5

More neutron-rich material is produced under these conditions with isotopic distributions skewed towards more neutron-rich isotopes.

This is due to the higher peak and average density conditions experienced in this model as compared with the mod.C.ar1d4 trajectory. The most overproduced isotope in trajectory mod.C.ar1d5 is ^{88}Sr , with an overproduction factor of 9.8×10^5 along with ^{87}Rb and $^{62,64}\text{Ni}$, all with overproduction factors of greater than 10^5 . A similar distribution is observed in the mod.D.ar1d5 model, however ^{64}Ni is the most overproduced isotope in this case, with ^{87}Rb , ^{86}Kr , ^{88}Sr and ^{54}Cr being the other isotopes with a production factor greater than 10^5 . A large number of isotopes in both the mod.C.ar1d5 and mod.D.ar1d5 models are overproduced by factors of $\sim 10^4 - 9$ for the mod.C.ar1d5 case and 12 for the mod.D.ar1d5, all of which are clustered around the iron group region. Temperatures in mod.C.ar1d5 have been clipped at 10 GK as reaction rate tables are not available beyond this value.

The overall distribution and range of production is similar between mod.C.ar1d5 and mod.D.ar1d5, as can be seen in the bottom right panel of Fig. 6 and Figs 8 and 9.

As discussed by Fryer et al. (2006), fall-back trajectories can produce r-process abundances with mild neutron-rich conditions. In the scenario discussed here, within a realistic range of accretion rates, mod.C.ar1d5 and mod.D.ar1d5 both show neutron-rich Y_e (0.447 and 0.443, respectively) and an abundance signature similar to the weak r-process (e.g. Seeger, Fowler & Clayton 1965; Kratz et al. 1993; Arcones & Montes 2011; Wanajo 2013). Collapsars, as investigated by Siegel, Barnes & Metzger (2018), with accretion rates from 0.3 to 30 times those investigated in these ar1d5 trajectories have also been shown to have an increase in neutron-rich material.

Panel (f) of Fig. 7 shows the integrated flux plot for the mod.C.ar1d5 trajectory. It can be seen that the reaction pathways for this trajectory are through more neutron-rich isotopes than in the mod.C.ar1d4 case. This is due to the higher density over the period of infall and ejection, making electron capture decays more efficient. In contrast to the mod.C.ar1d4 case [panel (e) of Fig. 7], the material is more neutron rich, due to the higher peak density and increased time spent at higher densities in this trajectory, favouring electron capture reactions in the accreted material.

4 IMPLICATIONS FOR GALACTIC CHEMICAL EVOLUTION

In the previous section we have explored the large variety of nucleosynthesis that can be found in material infalling close to the neutron star at different accretion rates, and ejected back in the stellar host, and into the interstellar medium following evolution of the companion star. Both light and heavy elements can be made, showing proton-rich or neutron-rich isotopic patterns by slightly changing the trajectory conditions within a realistic parameter space. Interestingly, all of the different nucleosynthesis patterns shown could be produced in the same merging event, during the evolution of the merging system. The toy model presented in Section 2 made to access the possible nucleosynthesis found in these systems is meant to be a first step to explore the production of elements in these systems, and motivate fully resolved hydrodynamics simulations. Based on the calculations present here, we can now also verify if these systems are relevant also for GCE.

4.1 Population synthesis study of CE phases

Before studying the role of these stellar objects in a GCE context, we need to determine the yields mass ejection in CE, and couple the accretion rates from Section 2 with the properties of the CE systems.

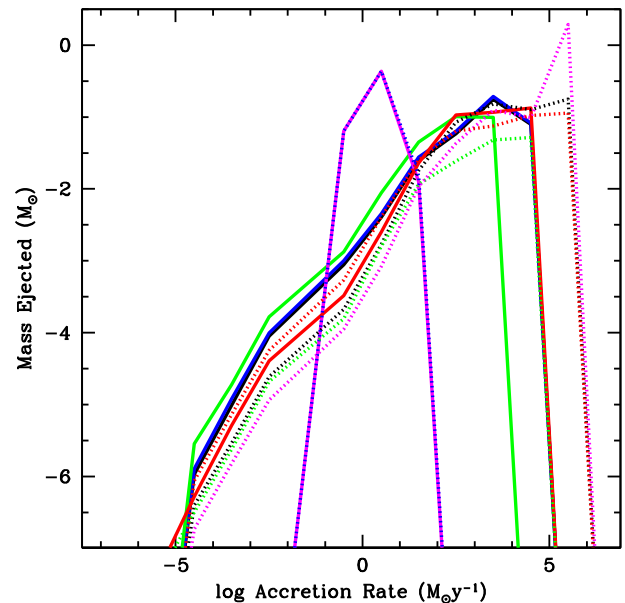


Figure 11. Mass ejected versus accretion rate for 10 sample binary systems in our population synthesis calculations. As the neutron star spirals into its companion, the accretion rate increases. Throughout this inspiral phase, mass is ejected and the conditions of this ejecta evolve as the neutron star spirals into deeper and deeper stellar layers. The peak accretion rate depends upon the structure of the stellar core and the depth of the inspiral.

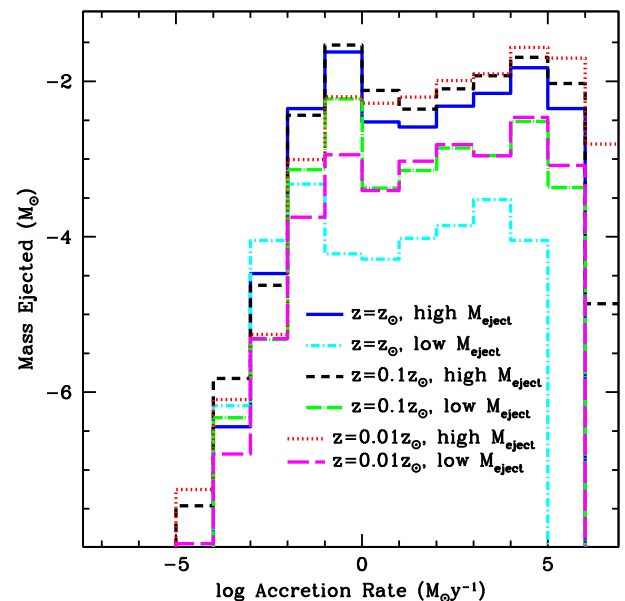


Figure 12. Average mass ejected per binary system (based on the population synthesis models) as a function of metallicity (solar, 1/10th solar, and 1/100th solar) for two extremes in our assumptions for accretion rate and mass ejected ('high' denotes $\lambda_{\text{BHL}} = 1/4$, 25 per cent mass ejecta, low denotes $\lambda_{\text{BHL}} = 1/40$, 10 per cent mass ejecta). Some binaries will not eject much mass at all, others will eject over a solar mass.

To study the population of CE phases, we employ the STARTRACK population synthesis code (Belczynski, Kalogera & Bulik 2002; Belczynski et al. 2008) to generate a population of binary compact objects. The code is based on revised formulas from Hurley, Pols & Tout (2000); updated with new wind mass-loss prescriptions,

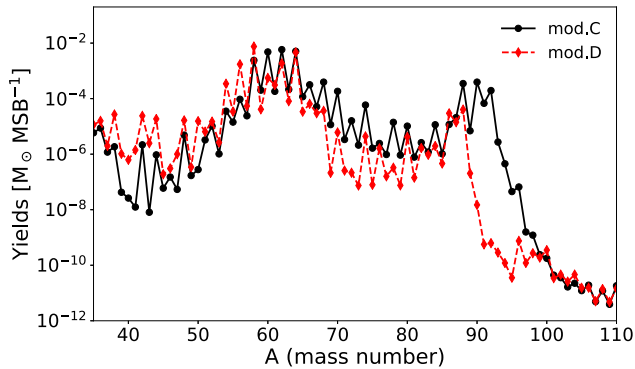


Figure 13. Yields ejected by CE events on average per massive-star binary (MSB) at $Z=0.02$, representing the convolution of our population synthesis models (Section 4.1) with the yields calculated for different accretion rates (see Section 3.1), using the trajectories ‘mod.C’ (black line) and ‘mod.D’ (red line). This is for $\lambda_{\text{BHL}} = 1/4$ and 25 per cent mass ejecta (see Section 4.1). The complete set of yields used in our GCE calculations for different metallicities and mass accretion and ejection options is available online at [CANFAR](#).

calibrated tidal interactions, physical estimation of donor’s binding energy in CE calculations and convection driven, neutrino enhanced supernova engines. A full description of these updates is given in Dominik et al. (2012). The two most recent updates take into account measurements of initial parameter distributions for massive O stars (Sana et al. 2012) as well as a correction of a technical bug that has limited the formation of BH–BH binaries for high metallicity (e.g. $Z = 0.02$).

With this code, we modelled the binary interactions of 500 000 stars for three different metallicities (Table 5). Only a small fraction of the systems actually go through a CE phase. For each of these systems, we calculate the progenitor star mass, the radius at the onset of the CE phase, and the final separation. Fig. 10 shows the distribution of initial vs final separations for these binary systems. Using the progenitor mass and radius at the onset of the CE phase, we can determine which of our MESA progenitors to use and the time in its evolution. There is a slight inconsistency in our approach, because the formulae for the stellar radii versus time in the population synthesis models are not identical to our MESA models, but this discrepancy allows us to make a first approximation of the accretion rates. Once we determine the mass and time of the CE interaction, we can use the final separation to determine how deep the neutron star inspirals into its companion.

With our stellar structures and the separation evolution, we can follow the full range of accretion rates in the CE phase. During the CE phase, the NS is continuously accreting and ejecting mass, evolving through a range of accretion rates as the NS spirals down towards the stellar core. The accretion and ejection is rapid compared to the CE phase, and we can approximate this evolution as a series of phases with different accretion rates. For each binary system in our population synthesis calculation, we know the mass of the stellar component, the evolutionary time-scale of the star at the initiation of CE phase (from the initial binary separation) and the range of accretion rates (based on the final binary separation and our stellar models). We then assume that 25 per cent of the accreted mass is reheated and ejected based on the results of accretion simulations (Fryer et al. 2006) to get the rate of mass ejection.

To get the total amount of mass ejected, we integrate the mass ejection rate over the inward spiral of the NS. Based on CE simulations (Ricker & Taam 2008, 2012; Passy et al. 2012; Ivanova et al. 2013), we assume that the duration of a typical CE phase persists for roughly three times the orbital period (P_{onset}) at the onset of the CE phase. In our calculations, we will assume that the time spent at each radius (t_r) is three times this orbital period (P_r) at radius r , for each bin i , normalized by the orbital period of each radius:

$$t_r = 3P_{\text{onset}}P(r_i) / \sum_i (P(r_i)). \quad (10)$$

In this paper, we consider three options for the mass accretion and ejection: $\lambda_{\text{BHL}} = 1/4$, 25 per cent mass ejecta, $\lambda_{\text{BHL}} = 1/40$, 25 per cent mass ejecta, and $\lambda_{\text{BHL}} = 1/40$, 10 per cent mass ejecta. Recall that λ_{BHL} is a non-dimensional parameter relating to the efficiency of accretion in our system (see Section 2.1). Fig. 11 shows the distribution of accretion rates for 10 of the close binaries in our population synthesis calculation with our model using $\lambda_{\text{BHL}} = 1/40$, 25 per cent mass ejecta.

Using our full population of binary systems, we can estimate the average mass ejected per binary system as a function of metallicity and our value for λ_{BHL} (Fig. 12). The fraction of merging systems in our models are 34 per cent, 61 per cent, and 75 per cent for 1, 0.1, and 0.01 solar metallicities, respectively. On average, a binary system ejects a few hundredths of a solar mass of material (in practice, some systems can eject nearly a solar mass of material while many systems eject very little mass).

Our MESA stellar models consist of a coarse grid in mass and time, which presents challenges in the outer layers of the companion star in matching with our population synthesis models, extracted from Hurley et al. (2000). This is not a concern however at higher accretion rates near the core of the companion, where the majority of burning in these models is observed, so long as the core masses of our stars are similar. As we focus on higher accretion rates for our yields, inconsistencies introduced by this are minimal in our models.

4.2 Galactic chemical evolution

To estimate the contribution of CE mass ejection events in a GCE context, we use the OMEGA code described in Côté et al. (2017). This is a classical one-zone open-box model (e.g. Tinsley 1980) that is part of the open-source NUPYCEE package.¹ We adopt the same default Milky Way set-up as in Côté et al. (2018). Our input parameters are tuned to reproduce the star formation rate, the gas fraction, the gas inflow rate, and the Type Ia and core-collapse supernova rates currently observed in the Milky Way (see table 1 in Kubryk, Prantzos & Athanassoula 2015), within the observational errors. Our model is also calibrated to reach solar metallicity ($Z_m = 0.014$, Asplund et al. 2009) when the Sun forms, which is 4.6 Gyr before the end of the simulation (Connelly, Bollard & Bizzarro 2017). The evolution of metallicity in our model is generated using NuGrid yields (Ritter et al. 2018) for massive and low-mass stars, and the yields of Iwamoto et al. (1999) for Type Ia supernovae.

To include the contribution of CE events, we use the NUPYCEE delayed-extra source implementation² which allows to include

¹<https://github.com/NuGrid/NuPyCEE>

²https://github.com/NuGrid/NuPyCEE/blob/master/DOC/Capabilities/Delayed_extra_sources.ipynb

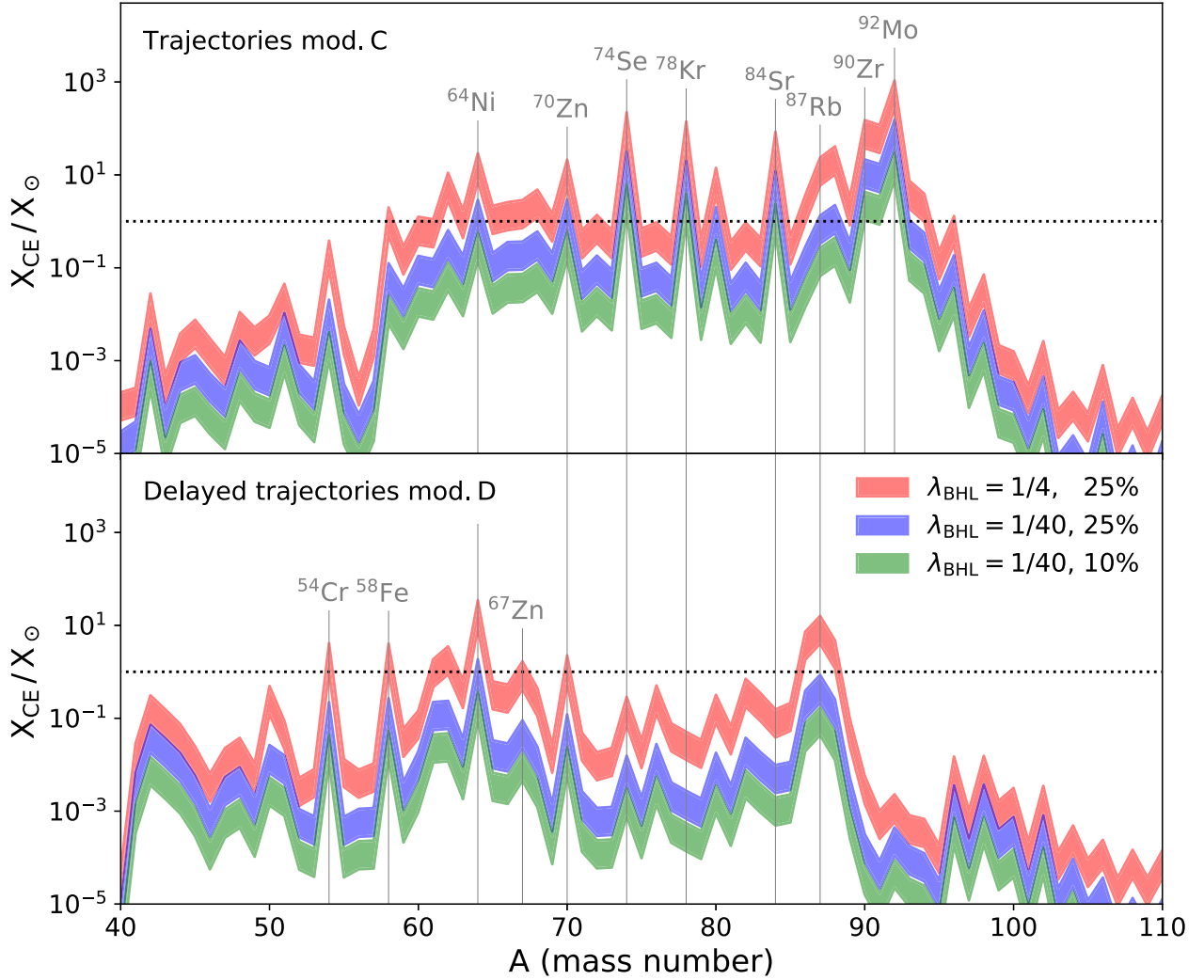


Figure 14. Contribution of CE events on the solar isotopic (mass number) composition of the Sun, using the GCE framework described in Section 4.2 and the yields from the trajectories ‘mod.C’ (top) and ‘mod.D’ (bottom). Different colours represent our different mass accretion and ejection options (see Section 4.1), where λ_{BHL} defines the magnitude of the accretion rates (see equation 3) and the percentage represent the fraction of accreted mass that is reheated and ejected. For each colour, the band represents the range of solutions assuming different binary fractions from 25 per cent to 100 per cent for massive stars. The dotted horizontal line shows a contribution of 100 per cent. Anything above this line implies an overestimation relative to the solar composition. Isotopes of interest which are overproduced are labelled.

additional enrichment sources based on input metallicity-dependent delay-time distribution functions and yields. Because the high NS accretion rate CE events studied here occur in systems involving two massive stars, the mass ejection rate is assumed to follow the lifetime of massive stars. In practical terms, for each stellar population formed in our model, all CE events occur between 5 and 40 Myr following the formation of the progenitor stars. This first-order implementation will be improved in follow-up studies. For the chemical composition of CE events ejecta, we convolve our nucleosynthesis calculations (see Section 3.1) with the metallicity-dependent mass ejection rates inferred from our population synthesis analysis (Section 4.1). An example of the resulting yields is shown in Fig. 13. The complete set of yields used in our chemical evolution calculations is available online at [CANFAR](#).

Fig. 14 shows the contribution of CE events to the solar isotopic composition predicted by our models, using our three mass

accretion and ejection options described in Section 4.1: $\lambda_{\text{BHL}} = 1/4$, 25 per cent mass ejecta, $\lambda_{\text{BHL}} = 1/40$, 25 per cent mass ejecta, and $\lambda_{\text{BHL}} = 1/40$, 10 per cent mass ejecta. We also varied the binary fraction of massive stars between 25 per cent and 100 per cent. Overall, the different mass accretion and ejection options cause more variations in our predictions than the binary fraction. Those figures show that in some cases, CE events could significantly contribute to the chemical evolution of some iron-peak and first-peak neutron-capture isotopes in the Galaxy. In fact, some isotopes are overproduced in our models relative to the solar composition. Our result here shows only the contributions from CE events to the solar composition, as direct comparison to isotopic abundances of other contributing events depends sensitively on the models chosen.

As mentioned in the previous sections, the nucleosynthesis of CE events is sensitive to the physical conditions (i.e. temperature and density). For example, when using the yields from the trajectories

‘mod.C.’, the p-isotopes ^{74}Se , ^{78}Kr , ^{84}Sr , and ^{92}Mo , as well as $^{90,91}\text{Zr}$, are always overestimated by more than an order of magnitude. However, when using the yields from the delayed trajectories ‘mod.D.’, none of these isotopes are significantly produced. Instead, the isotopes contributing the most to the solar compositions are rather in that case concentrated on the neutron-rich side, such as ^{64}Ni , ^{70}Zn , and ^{86}Kr .

We note that the nucleosynthesis has been calculated assuming an initial metallicity $Z = 0.014$, and that we used those yields for all metallicities. The purpose of our chemical evolution calculations is to verify whether or not CE events could be important for GCE. Our results should be seen as a first-order approximation and a motivation for future work.

5 FINAL DISCUSSION AND CONCLUSIONS

In this work we have explored the nucleosynthesis produced by neutron stars accreting in binary CEs. A realistic range of accretion rate conditions is explored (between 1 and $10^5 M_{\odot} \text{ yr}^{-1}$), for two sets of trajectories. In the first set, material is assumed to be near free-fall, and suddenly ejected with acceleration comparable (and in opposite direction) to the gravitational acceleration. In the second set, material is ejected with more gradual acceleration, resulting in lower temperature and density peaks compared to the first set. A large variety of nucleosynthesis patterns were obtained. Heavier elements are produced with increasing accretion rate, due to the higher temperature and density peaks. In particular, weak interactions become extremely important in defining the final composition at accretion rates of $10^4\text{--}10^5 M_{\odot} \text{ yr}^{-1}$, and leading to a proton-rich or neutron-rich nucleosynthesis pattern for heavy elements between Fe and Ru.

We test for the first time the impact of CE events in a GCE context. We find that accreting neutron stars could contribute in a non-negligible way to the solar composition for some isotopes. In particular, using yields from the first set of trajectories, we overproduce many p-isotopes such as ^{74}Se , ^{78}Kr , ^{84}Sr , and ^{92}Mo , among others. Using the second set of trajectories where there is a gradual change in trajectory, these events do not contribute to the solar abundances of these isotopes. The yields from these events is therefore highly dependent on the specific physical conditions experienced in the CE event, and the conditions in which the nucleosynthesis takes place is therefore crucial for GCE.

To summarize, we have shown that neutron stars accreting in binary CEs are potentially an important (unaccounted for) nucleosynthesis site for the chemical evolution of the Galaxy. Due to the simple approximations made in this first study for the nucleosynthesis trajectories, present sets of yields are still highly uncertain. But these results are a first important step, demanding more detailed simulations in the future.

ACKNOWLEDGEMENTS

NuGrid acknowledges support from National Science Foundation grant PHY-1430152 (JINA Center for the Evolution of the Elements) and Science and Technology Funding Council (through the University of Hull’s Consolidated Grant ST/R000840/1). MP and JK also acknowledge support by ongoing resource allocations on the University of Hull’s High Performance Computing Facility viper.

BC acknowledges support from the European Research Council Consolidator Grant (Hungary) funding scheme (project RADIOSTAR, G.A. n. 724560).

KB acknowledges support from the Polish National Science Center (NCN) grants Sonata Bis 2 (DEC-2012/07/E/ST9/01360), OPUS (2015/19/B/ST9/01099), Maestro (2015/18/A/ST9/00746, and LOFT/eXTP 2013/10/M/ST9/00729).

This work was, in part, supported by the US Department of Energy through the Los Alamos National Laboratory. Additional funding was provided by the Laboratory Directed Research and Development Program and the Center for Nonlinear Studies at Los Alamos National Laboratory under project number 20170508DR.

REFERENCES

- Abbott B. P. et al., 2017, *ApJ*, 848, L12
 Angulo C. et al., 1999, *Nucl. Phys. A*, 656, 3
 Arcones A., Montes F., 2011, *ApJ*, 731, 5
 Arnould M., Goriely S., 2003, *Phys. Rep.*, 384, 1
 Asplund M., Grevesse N., Sauval A. J., Scott P., 2009, *ARA&A*, 47, 481
 Belczynski K., Kalogera V., Bulik T., 2002, *ApJ*, 572, 407
 Belczynski K., Kalogera V., Rasio F. A., Taam R. E., Zezas A., Bulik T., Maccarone T. J., Ivanova N., 2008, *ApJS*, 174, 223
 Bloom J. S., Sigurdsson S., Pols O. R., 1999, *MNRAS*, 305, 763
 Bondi H., 1952, *MNRAS*, 112, 195
 Caughlan G. R., Fowler W. A., 1988, *At. Data Nucl. Data Tables*, 40, 283
 Champagne A. E., Wiescher M., 1992, *Annu. Rev. Nucl. Part. Sci.*, 42, 39
 Chevalier R. A., 1989, *ApJ*, 346, 847
 Chevalier R. A., 1993, *ApJ*, 411, L33
 Connelly J. N., Bollard J., Bizzarro M., 2017, *Geochim. Cosmochim. Acta*, 201, 345
 Côté B., O’Shea B. W., Ritter C., Herwig F., Venn K. A., 2017, *ApJ*, 835, 128
 Côté B., Denissenkov P., Herwig F., Ruiter A. J., Ritter C., Pignatari M., Belczynski K., 2018, *ApJ*, 854, 105
 Cox A. N., Vauclair S., Zahn J. P., eds, 1983, *Astrophysical process in upper main sequence stars*
 Cyburt R., 2011, in *APS Division of Nuclear Physics Meeting Abstracts*, American Physical Society, p. 7
 Dillmann I., Heil M., Käppeler F., Plag R., Rauscher T., Thielemann F.-K., 2006, in *Woehr A., Aprahamian A., eds, AIP Conf. Proc. Vol. 819, Capture Gamma-Ray Spectroscopy and Related Topics*. Am. Inst. Phys., New York, p. 123
 Dominik M., Belczynski K., Fryer C., Holz D. E., Berti E., Bulik T., Mandel L., O’Shaughnessy R., 2012, *ApJ*, 759, 52
 Dominik M., Belczynski K., Fryer C., Holz D. E., Berti E., Bulik T., Mandel L., O’Shaughnessy R., 2013, *ApJ*, 779, 72
 Dominik M. et al., 2015, *ApJ*, 806, 263
 Fröhlich C., Martínez-Pinedo G., Liebendörfer M., Thielemann F.-K., Bravo E., Hix W. R., Langanke K., Zinner N. T., 2006, *Phys. Rev. Lett.*, 96, 142502
 Fryer C. L., 2009, *ApJ*, 699, 409
 Fryer C. L., Woosley S. E., 1998, *ApJ*, 502, L9
 Fryer C. L., Young P. A., 2007, *ApJ*, 659, 1438
 Fryer C. L., Benz W., Herant M., 1996, *ApJ*, 460, 801
 Fryer C. L., Colgate S. A., Pinto P. A., 1999a, *ApJ*, 511, 885
 Fryer C. L., Woosley S. E., Hartmann D. H., 1999b, *ApJ*, 526, 152
 Fryer C. L., Herwig F., Hungerford A., Timmes F. X., 2006, *ApJ*, 646, L131
 Fryer C. L., Belczynski K., Berger E., Thöne C., Ellinger C., Bulik T., 2013, *ApJ*, 764, 181
 Fuller G. M., Fowler W. A., Newman M. J., 1985, *ApJ*, 293, 1
 Fynbo H. O. U. et al., 2005, *Nature*, 433, 136
 Goriely S., 1999, *A&A*, 342, 881
 Heil M. et al., 2008, *Phys. Rev. C*, 78, 025803
 Hoyle F., Lyttleton R. A., 1941, *MNRAS*, 101, 227
 Hurley J. R., Pols O. R., Tout C. A., 2000, *MNRAS*, 315, 543
 Iliadis C., D’Auria J. M., Starrfield S., Thompson W. J., Wiescher M., 2001, *ApJS*, 134, 151

- Imbriani G. et al., 2005, *Eur. Phys. J. A*, 25, 455
- Ivanova N. et al., 2013, *A&AR*, 21, 59
- Iwamoto K., Brachwitz F., Nomoto K., Kishimoto N., Umeda H., Hix W. R., Thielemann F.-K., 1999, *ApJS*, 125, 439
- Jaeger M., Kunz R., Mayer A., Hammer J. W., Staudt G., Kratz K. L., Pfeiffer B., 2001, *Phys. Rev. Lett.*, 87, 202501
- Jones S. et al., 2013, *ApJ*, 772, 150
- Kiminki D. C. et al., 2007, *ApJ*, 664, 1102
- Kiminki D. C., Kobulnicky H. A., Gilbert I., Bird S., Chunev G., 2009, *AJ*, 137, 4608
- Kiminki D. C., Kobulnicky H. A., 2012, *ApJ*, 751, 4
- Kobulnicky H. A., Fryer C. L., 2007, *ApJ*, 670, 747
- Kobulnicky H. A. et al., 2014, *ApJS*, 213, 34
- Kratz K.-L., Bitouzet J.-P., Thielemann F.-K., Moeller P., Pfeiffer B., 1993, *ApJ*, 403, 216
- Kubryk M., Prantzos N., Athanassoula E., 2015, *A&A*, 580, A126
- Kunz R., Fey M., Jaeger M., Mayer A., Hammer J. W., Staudt G., Harissopulos S., Paradellis T., 2002, *ApJ*, 567, 643
- Langanke K., Martínez-Pinedo G., 2000, *Nucl. Phys. A*, 673, 481
- MacLeod M., Ramirez-Ruiz E., 2014, *ApJ*, 798, L19
- MacLeod M., Ramirez-Ruiz E., 2015, in *APS April Meeting Abstracts*, U2.004
- MacLeod M., Antoni A., Murguia-Berthier A., Macias P., Ramirez-Ruiz E., 2017, *ApJ*, 838, 56
- Murguia-Berthier A., MacLeod M., Ramirez-Ruiz E., Antoni A., Macias P., 2017, *ApJ*, 845, 173
- Oda T., Hino M., Muto K., Takahara M., Sato K., 1994, *At. Data Nucl. Data Tables*, 56, 231
- Passy J.-C. et al., 2012, *ApJ*, 744, 52
- Paxton B. et al., 2013, *ApJS*, 208, 4
- Paxton B. et al., 2015, *ApJS*, 220, 15
- Paxton B. et al., 2018, *ApJS*, 234, 34
- Paxton B., Bildsten L., Dotter A., Herwig F., Lesaffre P., Timmes F., 2011, *ApJS*, 192, 3
- Pignatari M. et al., 2016, *ApJS*, 225, 24
- Popham R., Woosley S. E., Fryer C., 1999, *ApJ*, 518, 356
- Rauscher T., Dauphas N., Dillmann I., Fröhlich C., Fülöp Z., Gyürky G., 2013, *Rep. Prog. Phys.*, 76, 066201
- Ricker P. M., Taam R. E., 2008, *ApJ*, 672, L41
- Ricker P. M., Taam R. E., 2012, *ApJ*, 746, 74
- Ritter C., Herwig F., Jones S., Pignatari M., Fryer C., Hirschi R., 2018, *MNRAS*, 480, 538
- Roberts L. F., Woosley S. E., Hoffman R. D., 2010, *ApJ*, 722, 954
- Ruffert M., 1994a, *A&AS*, 106, 505
- Ruffert M., 1994b, *ApJ*, 427, 342
- Ruffert M., Arnett D., 1994, *ApJ*, 427, 351
- Sana H. et al., 2012, *Science*, 337, 444
- Schatz H. et al., 2001, *Phys. Rev. Lett.*, 86, 3471
- Seeger P. A., Fowler W. A., Clayton D. D., 1965, *ApJS*, 11, 121
- Siegel D. M., Barnes J., Metzger B. D., 2018, preprint ([arXiv:1810.00098](https://arxiv.org/abs/1810.00098))
- Soker N., Gilkis A., 2018, *MNRAS*, 475, 1198
- Thorne K. S., Zytkow A. N., 1975, *ApJ*, 199, L19
- Tinsley B. M., 1980, *Fundam. Cosm. Phys.*, 5, 287
- Wanajo S., 2013, *ApJ*, 770, L22
- Zhang W., Fryer C. L., 2001, *ApJ*, 550, 357

SUPPORTING INFORMATION

Supplementary data are available at [CANFAR](https://www.cambridge.org/core) online.

Please note: Oxford University Press is not responsible for the content or functionality of any supporting materials supplied by the authors. Any queries (other than missing material) should be directed to the corresponding author for the article.

APPENDIX

Table A1. Abundances for trajectories mod.C.ar1d0, mod.C.ar1d1, mod.C.ar1d2, mod.C.ar1d3, mod.C.ar1d4, and mod.C.ar1d5, respectively, up to isotope ^{50}V . Complete tables are available online. Final electron fractions (Y_e) are provided at the end of the table.

Element	A	$1 M_{\odot} \text{ yr}^{-1}$	$10 M_{\odot} \text{ yr}^{-1}$	$10^2 M_{\odot} \text{ yr}^{-1}$	$10^3 M_{\odot} \text{ yr}^{-1}$	$10^4 M_{\odot} \text{ yr}^{-1}$	$10^5 M_{\odot} \text{ yr}^{-1}$
H	1	7.27e-01	7.27e-01	7.27e-01	7.24e-01	9.71e-12	1.27e-21
H	2	2.20e-18	2.39e-18	2.60e-18	2.81e-18	2.39e-25	4.72e-34
He	3	7.20e-12	3.44e-15	5.93e-15	1.16e-14	3.42e-29	3.15e-24
He	4	2.59e-01	2.54e-01	2.23e-01	1.44e-01	5.03e-02	9.54e-06
Li	7	3.99e-05	4.68e-10	4.17e-11	2.09e-11	6.79e-21	3.61e-23
B	11	5.77e-10	4.91e-15	3.18e-16	9.10e-17	6.25e-32	2.15e-31
C	12	2.60e-09	1.30e-11	7.56e-12	8.86e-12	3.00e-05	3.03e-12
C	13	2.67e-07	1.08e-09	8.62e-10	2.75e-10	1.30e-11	4.91e-27
N	14	1.27e-06	1.88e-06	2.11e-06	1.08e-06	2.76e-18	1.04e-26
N	15	2.98e-04	1.21e-08	4.00e-08	5.89e-08	1.22e-18	8.35e-16
O	16	2.54e-07	2.48e-09	1.08e-08	1.71e-08	6.14e-08	1.12e-11
O	17	6.08e-08	7.24e-09	2.15e-09	2.56e-10	1.69e-17	5.65e-23
O	18	2.68e-03	1.10e-05	1.40e-05	7.64e-06	1.86e-23	5.20e-24
F	19	8.83e-08	7.62e-12	2.44e-11	3.36e-11	8.00e-19	6.47e-17
Ne	20	2.57e-05	5.33e-08	1.05e-07	1.01e-07	7.16e-08	3.38e-13
Ne	21	3.60e-04	1.72e-09	2.08e-09	5.11e-09	4.37e-14	6.95e-21
Ne	22	4.77e-03	9.40e-06	7.06e-06	1.56e-06	1.44e-17	1.69e-16
Na	23	3.70e-04	9.51e-06	1.90e-05	1.33e-05	1.06e-11	4.17e-15
Mg	24	1.69e-03	2.53e-05	4.08e-05	2.80e-05	4.66e-08	1.73e-14
Mg	25	2.05e-05	1.77e-07	7.95e-07	1.46e-06	4.15e-13	5.87e-16
Mg	26	8.21e-08	1.16e-07	2.25e-09	4.39e-09	2.20e-10	2.12e-14
Al	27	5.67e-04	1.34e-04	3.88e-05	2.06e-05	5.77e-08	3.16e-14
Si	28	2.77e-04	6.40e-04	1.47e-04	8.13e-05	6.38e-08	6.26e-15
Si	29	1.36e-08	4.16e-05	5.47e-08	6.50e-08	3.47e-09	8.51e-14
Si	30	1.79e-06	1.02e-06	6.21e-09	3.47e-09	4.32e-07	2.49e-13
P	31	5.47e-04	4.39e-03	9.98e-05	5.76e-05	2.16e-08	7.18e-15
S	32	6.98e-05	7.98e-03	1.50e-04	8.73e-05	3.05e-07	2.40e-13
S	33	3.07e-04	8.05e-04	1.45e-06	2.21e-06	9.65e-08	6.35e-14
S	34	1.17e-08	6.46e-05	3.48e-07	2.64e-08	1.30e-06	1.19e-12
S	36	7.00e-99	7.00e-99	4.63e-35	2.73e-35	5.05e-10	2.51e-13
Cl	35	1.36e-08	1.62e-03	1.86e-04	1.11e-04	2.53e-07	3.84e-14
Cl	37	4.47e-05	2.05e-04	8.47e-07	1.19e-06	1.38e-07	3.33e-13
Ar	36	2.38e-06	2.43e-03	2.56e-04	1.57e-04	7.30e-07	1.40e-14
Ar	38	8.44e-10	1.79e-04	1.84e-04	1.06e-04	4.36e-06	3.22e-12
Ar	40	2.42e-33	3.44e-39	4.52e-35	7.19e-39	8.07e-09	5.48e-13
K	39	2.32e-08	3.77e-07	3.66e-06	4.13e-06	2.97e-07	3.07e-14
K	40	3.46e-27	4.09e-28	8.11e-28	1.38e-27	1.88e-08	3.81e-15
K	41	8.10e-09	2.45e-06	2.11e-07	3.90e-07	2.20e-07	7.32e-14
Ca	40	1.09e-10	7.40e-08	1.10e-06	1.17e-06	1.34e-06	1.18e-16
Ca	42	5.99e-05	5.05e-05	1.81e-04	7.80e-05	9.18e-06	9.35e-14
Ca	43	1.46e-08	1.12e-07	3.01e-07	3.46e-07	4.04e-07	1.39e-13
Ca	44	3.65e-07	1.37e-05	1.01e-04	8.75e-05	1.27e-06	9.41e-13
Ca	46	9.00e-99	9.00e-99	9.00e-99	5.28e-37	7.65e-14	2.04e-11
Ca	48	8.00e-99	8.00e-99	8.00e-99	2.96e-38	1.26e-21	6.82e-11
Sc	45	1.16e-08	6.51e-08	9.97e-07	1.96e-06	4.01e-06	2.08e-13
Ti	46	1.68e-07	8.36e-08	1.18e-05	9.79e-07	8.96e-06	3.76e-14
Ti	47	5.35e-08	1.98e-07	3.47e-06	3.55e-06	1.72e-06	2.35e-11
Ti	48	2.32e-08	6.27e-07	6.72e-04	3.89e-04	7.55e-06	5.11e-09
Ti	49	7.77e-08	7.82e-08	5.66e-06	8.81e-06	8.71e-06	1.66e-08
Ti	50	1.00e-98	1.00e-98	1.00e-98	1.60e-24	7.33e-12	2.18e-05
V	50	1.00e-99	1.00e-99	1.00e-99	4.25e-29	3.54e-08	1.01e-09
Y_{efin}	N/A	8.64e-01	8.63e-01	8.63e-01	8.61e-01	4.68e-01	4.47e-01

Table A2. The same as Table A1, but for trajectories mod.D.ar1d0, mod.D.ar1d1, mod.D.ar1d2, mod.D.ar1d3, mod.D.ar1d4, and mod.D.ar1d5, respectively.

Element	A	$1 M_{\odot} \text{ yr}^{-1}$	$10 M_{\odot} \text{ yr}^{-1}$	$10^2 M_{\odot} \text{ yr}^{-1}$	$10^3 M_{\odot} \text{ yr}^{-1}$	$10^4 M_{\odot} \text{ yr}^{-1}$	$10^5 M_{\odot} \text{ yr}^{-1}$
H	1	7.28e-01	7.27e-01	7.26e-01	7.25e-01	2.79e-01	2.92e-23
H	2	2.20e-18	2.39e-18	2.60e-18	2.81e-18	1.07e-18	1.13e-34
He	3	3.49e-11	1.02e-14	5.71e-15	1.12e-14	3.65e-15	1.58e-23
He	4	2.61e-01	2.58e-01	2.42e-01	1.57e-01	8.04e-02	6.70e-07
Li	7	6.22e-05	2.13e-06	2.45e-11	1.54e-11	1.90e-11	5.18e-24
B	11	7.91e-10	2.28e-11	2.03e-16	7.38e-17	4.50e-17	4.72e-30
C	12	4.92e-09	6.21e-11	9.70e-12	1.14e-11	1.74e-11	6.18e-13
C	13	4.07e-07	3.33e-08	1.11e-09	3.62e-10	1.22e-10	1.25e-24
N	14	1.90e-03	2.34e-06	2.59e-06	1.36e-06	3.90e-07	3.78e-22
N	15	5.68e-04	2.13e-06	5.10e-08	7.54e-08	5.32e-08	2.42e-16
O	16	5.68e-07	1.23e-06	1.46e-08	2.09e-08	2.92e-09	1.41e-12
O	17	5.75e-06	8.21e-09	2.87e-09	3.52e-10	2.20e-10	5.56e-21
O	18	5.10e-03	2.14e-05	1.78e-05	9.78e-06	2.95e-06	8.34e-23
F	19	1.49e-07	5.69e-10	3.13e-11	4.32e-11	3.11e-11	5.27e-18
Ne	20	3.91e-07	3.31e-05	1.43e-07	1.24e-07	1.66e-08	4.38e-15
Ne	21	2.44e-06	4.38e-04	2.69e-09	6.21e-09	1.92e-09	3.73e-19
Ne	22	8.73e-04	5.74e-05	9.60e-06	2.10e-06	8.16e-07	2.41e-18
Na	23	5.11e-06	2.56e-03	3.06e-05	1.68e-05	4.64e-06	8.55e-17
Mg	24	2.15e-05	6.82e-03	6.57e-05	3.54e-05	9.73e-06	9.50e-17
Mg	25	2.58e-06	4.82e-04	1.30e-06	1.85e-06	1.20e-06	9.90e-18
Mg	26	5.72e-08	1.90e-06	3.64e-09	5.55e-09	3.71e-09	2.55e-16
Al	27	5.22e-04	5.60e-04	7.50e-05	2.68e-05	7.86e-06	3.12e-16
Si	28	6.36e-05	1.97e-03	2.87e-04	1.05e-04	3.27e-05	1.46e-16
Si	29	2.18e-08	6.16e-08	1.57e-07	8.60e-08	7.09e-08	4.47e-16
Si	30	2.07e-06	7.29e-07	1.11e-08	4.61e-09	5.70e-09	2.22e-14
P	31	6.08e-04	3.01e-04	2.69e-04	7.81e-05	2.20e-05	2.76e-16
S	32	6.52e-06	3.34e-04	4.06e-04	1.18e-04	3.41e-05	1.61e-15
S	33	3.06e-04	3.07e-04	4.59e-06	2.99e-06	2.01e-06	5.10e-15
S	34	3.97e-09	7.29e-08	5.65e-06	3.99e-08	1.81e-08	1.72e-13
S	36	3.98e-31	2.21e-34	1.75e-35	2.49e-35	2.45e-35	1.39e-12
Cl	35	8.35e-07	5.31e-08	2.70e-03	1.67e-04	4.25e-05	8.99e-15
Cl	37	4.48e-05	4.50e-05	3.33e-04	1.89e-06	1.20e-06	1.46e-13
Ar	36	1.47e-06	2.49e-06	3.72e-03	2.36e-04	6.26e-05	9.50e-17
Ar	38	1.62e-09	2.35e-09	6.93e-03	1.69e-04	4.22e-05	3.66e-13
Ar	40	8.39e-31	9.21e-34	2.06e-35	7.71e-36	3.66e-35	7.49e-13
K	39	2.40e-08	2.01e-08	2.64e-04	7.14e-06	1.03e-06	9.58e-15
K	40	9.24e-22	3.28e-29	1.00e-99	2.93e-27	2.07e-27	7.28e-17
K	41	2.78e-06	5.34e-08	3.71e-04	6.61e-07	2.79e-07	7.05e-15
Ca	40	2.22e-05	1.12e-10	8.46e-05	2.05e-06	1.45e-07	9.98e-20
Ca	42	3.42e-05	5.62e-05	5.95e-03	1.32e-04	5.94e-05	6.79e-14
Ca	43	2.30e-08	3.73e-08	6.71e-04	6.01e-07	5.51e-07	1.81e-13
Ca	44	1.67e-07	4.06e-06	4.76e-03	1.48e-04	1.20e-05	3.79e-11
Ca	46	4.26e-26	9.00e-99	9.00e-99	6.41e-37	8.43e-37	1.32e-08
Ca	48	2.89e-29	8.00e-99	8.00e-99	8.00e-99	8.00e-99	4.03e-07
Sc	45	4.49e-08	5.72e-08	4.29e-05	3.32e-06	1.05e-06	2.25e-11
Ti	46	6.65e-09	5.51e-08	2.87e-05	1.75e-06	1.73e-05	5.48e-13
Ti	47	2.57e-07	2.90e-07	2.54e-04	6.26e-06	2.45e-06	5.54e-09
Ti	48	9.20e-07	1.68e-07	2.89e-03	7.22e-04	1.42e-04	3.65e-08
Ti	49	4.63e-07	7.25e-08	3.25e-05	1.67e-05	7.03e-06	4.13e-06
Ti	50	2.52e-11	2.80e-32	1.40e-35	1.01e-36	8.80e-24	1.59e-03
V	50	7.96e-09	1.00e-99	1.00e-99	9.80e-29	8.00e-27	2.95e-09
Y_{fin}	N/A	8.64e-01	8.63e-01	8.63e-01	8.62e-01	6.37e-01	4.42e-01

Table A3. Overproduction factors for all accretion rates for trajectories mod.C.ar1d0, mod.C.ar1d1, mod.C.ar1d2, mod.C.ar1d3 mod.C.ar1d4, and mod.C.ar1d5, respectively, up to isotope ^{50}V . Complete tables are available online at [CANFAR](#).

Element	A	$1 M_{\odot} \text{ yr}^{-1}$	$10 M_{\odot} \text{ yr}^{-1}$	$10^2 M_{\odot} \text{ yr}^{-1}$	$10^3 M_{\odot} \text{ yr}^{-1}$	$10^4 M_{\odot} \text{ yr}^{-1}$	$10^5 M_{\odot} \text{ yr}^{-1}$
H	1	9.98e-01	9.97e-01	9.98e-01	9.93e-01	1.33e-11	1.74e-21
H	2	1.56e-13	1.69e-13	1.84e-13	1.99e-13	1.69e-20	3.34e-29
He	3	1.66e-07	7.93e-11	1.37e-10	2.68e-10	7.88e-25	7.26e-20
He	4	9.93e-01	9.71e-01	8.54e-01	5.50e-01	1.93e-01	3.65e-05
Li	7	9.16e+05	1.07e+01	9.57e-01	4.79e-01	1.56e-10	8.28e-13
B	11	2.17e-01	1.85e-06	1.20e-07	3.43e-08	2.36e-23	8.12e-23
C	12	1.49e-06	7.44e-09	4.33e-09	5.07e-09	1.71e-02	1.73e-09
C	13	1.26e-02	5.08e-05	4.06e-05	1.30e-05	6.13e-07	2.31e-22
N	14	2.51e-03	3.73e-03	4.18e-03	2.15e-03	5.47e-15	2.06e-23
N	15	1.50e+02	6.06e-03	2.01e-02	2.96e-02	6.15e-13	4.20e-10
O	16	5.80e-05	5.66e-07	2.47e-06	3.91e-06	1.40e-05	2.56e-09
O	17	3.51e-02	4.17e-03	1.24e-03	1.48e-04	9.75e-12	3.26e-17
O	18	2.71e+02	1.12e+00	1.42e+00	7.73e-01	1.88e-18	5.27e-19
F	19	2.13e-01	1.84e-05	5.90e-05	8.13e-05	1.93e-12	1.56e-10
Ne	20	3.33e-02	6.91e-05	1.37e-04	1.31e-04	9.28e-05	4.38e-10
Ne	21	1.85e+02	8.84e-04	1.07e-03	2.63e-03	2.25e-08	3.58e-15
Ne	22	7.64e+01	1.51e-01	1.13e-01	2.49e-02	2.31e-13	2.71e-12
Na	23	1.81e+01	4.66e-01	9.31e-01	6.50e-01	5.21e-07	2.04e-10
Mg	24	4.40e+00	6.57e-02	1.06e-01	7.26e-02	1.21e-04	4.48e-11
Mg	25	4.03e-01	3.47e-03	1.56e-02	2.87e-02	8.16e-09	1.15e-11
Mg	26	1.41e-03	1.99e-03	3.86e-05	7.54e-05	3.77e-06	3.65e-10
Al	27	1.49e+01	3.53e+00	1.02e+00	5.42e-01	1.52e-03	8.32e-10
Si	28	5.52e-01	1.28e+00	2.93e-01	1.62e-01	1.27e-04	1.25e-11
Si	29	5.14e-04	1.58e+00	2.07e-03	2.46e-03	1.31e-04	3.23e-09
Si	30	9.94e-02	5.68e-02	3.45e-04	1.93e-04	2.40e-02	1.38e-08
P	31	1.28e+02	1.03e+03	2.34e+01	1.35e+01	5.07e-03	1.69e-09
S	32	2.77e-01	3.17e+01	5.95e-01	3.47e-01	1.21e-03	9.53e-10
S	33	1.50e+02	3.92e+02	7.09e-01	1.08e+00	4.71e-02	3.10e-08
S	34	9.84e-04	5.44e+00	2.93e-02	2.23e-03	1.10e-01	9.98e-08
S	36	1.38e-91	1.38e-91	9.14e-28	5.38e-28	9.96e-03	4.94e-06
Cl	35	2.70e-03	3.21e+02	3.70e+01	2.21e+01	5.04e-02	7.63e-09
Cl	37	2.63e+01	1.20e+02	4.98e-01	6.99e-01	8.10e-02	1.96e-07
Ar	36	8.61e-02	8.80e+01	9.26e+00	5.66e+00	2.64e-02	5.06e-10
Ar	38	1.59e-04	3.37e+01	3.47e+01	2.00e+01	8.21e-01	6.06e-07
Ar	40	2.71e-25	3.85e-31	5.05e-27	8.05e-31	9.03e-01	6.13e-05
K	39	8.83e-03	1.43e-01	1.40e+00	1.57e+00	1.13e-01	1.17e-08
K	40	1.03e-17	1.21e-18	2.41e-18	4.09e-18	5.58e+01	1.13e-05
K	41	4.07e-02	1.23e+01	1.06e+00	1.96e+00	1.10e+00	3.68e-07
Ca	40	2.30e-06	1.56e-03	2.32e-02	2.46e-02	2.83e-02	2.49e-12
Ca	42	1.80e+02	1.52e+02	5.44e+02	2.34e+02	2.76e+01	2.81e-07
Ca	43	2.05e-01	1.58e+00	4.23e+00	4.86e+00	5.68e+00	1.96e-06
Ca	44	3.24e-01	1.22e+01	8.99e+01	7.78e+01	1.13e+00	8.37e-07
Ca	46	3.99e-90	3.99e-90	3.99e-90	2.34e-28	3.39e-05	9.05e-03
Ca	48	7.27e-92	7.27e-92	7.27e-92	2.69e-31	1.15e-14	6.20e-04
Sc	45	3.82e-01	2.15e+00	3.29e+01	6.48e+01	1.32e+02	6.87e-06
Ti	46	9.30e-01	4.62e-01	6.51e+01	5.41e+00	4.95e+01	2.08e-07
Ti	47	3.21e-01	1.19e+00	2.08e+01	2.13e+01	1.03e+01	1.41e-04
Ti	48	1.37e-02	3.72e-01	3.99e+02	2.31e+02	4.48e+00	3.03e-03
Ti	49	6.15e-01	6.19e-01	4.48e+01	6.97e+01	6.89e+01	1.31e-01
Ti	50	8.09e-92	8.09e-92	8.09e-92	1.29e-17	5.93e-05	1.77e+02
V	50	1.33e-90	1.33e-90	1.33e-90	5.67e-20	4.72e+01	1.35e+00

Table A4. The same as Table A3, but for trajectories mod.D.ar1d0, mod.D.ar1d1, mod.D.ar1d2, mod.D.ar1d3, mod.D.ar1d4, and mod.D.ar1d5, respectively.

Element	A	$1M_{\odot} \text{ yr}^{-1}$	$10M_{\odot} \text{ yr}^{-1}$	$10^2 M_{\odot} \text{ yr}^{-1}$	$10^3 M_{\odot} \text{ yr}^{-1}$	$10^4 M_{\odot} \text{ yr}^{-1}$	$10^5 M_{\odot} \text{ yr}^{-1}$
H	1	9.98e-01	9.97e-01	9.97e-01	9.94e-01	3.83e-01	4.00e-23
H	2	1.56e-13	1.69e-13	1.84e-13	1.99e-13	7.55e-14	8.00e-30
He	3	8.04e-07	2.35e-10	1.32e-10	2.59e-10	8.43e-11	3.64e-19
He	4	1.00e+00	9.89e-01	9.28e-01	6.03e-01	3.08e-01	2.56e-06
Li	7	1.43e+06	4.90e+04	5.64e-01	3.55e-01	4.37e-01	1.19e-13
B	11	2.98e-01	8.59e-03	7.67e-08	2.78e-08	1.70e-08	1.78e-21
C	12	2.81e-06	3.55e-08	5.55e-09	6.50e-09	9.96e-09	3.54e-10
C	13	1.92e-02	1.57e-03	5.21e-05	1.71e-05	5.75e-06	5.88e-20
N	14	3.77e+00	4.65e-03	5.14e-03	2.70e-03	7.73e-04	7.49e-19
N	15	2.86e+02	1.07e+00	2.57e-02	3.79e-02	2.68e-02	1.22e-10
O	16	1.30e-04	2.80e-04	3.34e-06	4.77e-06	6.68e-07	3.23e-10
O	17	3.32e+00	4.73e-03	1.66e-03	2.03e-04	1.27e-04	3.21e-15
O	18	5.17e+02	2.16e+00	1.81e+00	9.90e-01	2.99e-01	8.44e-18
F	19	3.59e-01	1.37e-03	7.56e-05	1.04e-04	7.50e-05	1.27e-11
Ne	20	5.06e-04	4.29e-02	1.86e-04	1.61e-04	2.114e-05	5.68e-12
Ne	21	1.26e+00	2.25e+02	1.38e-03	3.20e-03	9.87e-04	1.92e-13
Ne	22	1.40e+01	9.19e-01	1.54e-01	3.37e-02	1.31e-02	3.87e-14
Na	23	2.50e-01	1.25e+02	1.50e+00	8.24e-01	2.27e-01	4.19e-12
Mg	24	5.58e-02	1.77e+01	1.70e-01	9.19e-02	2.52e-02	2.46e-13
Mg	25	5.07e-02	9.47e+00	2.56e-02	3.63e-02	2.37e-02	1.95e-13
Mg	26	9.82e-04	3.27e+00	6.25e-05	9.55e-05	6.38e-05	4.38e-12
Al	27	1.37e+01	1.47e+01	1.97e+00	7.04e-01	2.07e-01	8.22e-12
Si	28	1.27e-01	3.94e+00	5.73e-01	2.10e-01	6.51e-02	2.92e-13
Si	29	8.27e-04	2.34e-03	5.96e-03	3.26e-03	2.69e-03	1.69e-11
Si	30	1.15e-01	4.06e-02	6.20e-04	2.56e-04	3.17e-04	1.23e-09
P	31	1.43e+02	7.07e+01	6.32e+01	1.83e+01	5.16e+00	6.48e-11
S	32	2.59e-02	1.33e+00	1.61e+00	4.70e-01	1.35e-01	6.40e-12
S	33	1.49e+02	1.50e+02	2.24e+00	1.46e+00	9.79e-01	2.49e-09
S	34	3.35e-04	6.14e-03	4.76e-01	3.36e-03	1.52e-03	1.45e-08
S	36	7.84e-24	4.36e-27	3.46e-28	4.91e-28	4.83e-28	2.74e-05
Cl	35	1.66e-01	1.05e-02	5.37e+02	3.33e+01	8.44e+00	1.79e-09
Cl	37	2.63e+01	2.65e+01	1.96e+02	1.11e+00	7.07e-01	8.61e-08
Ar	36	5.31e-02	9.01e-02	1.34e+02	8.52e+00	2.26e+00	3.43e-12
Ar	38	3.05e-04	4.42e-04	1.30e+03	3.18e+01	7.95e+00	6.90e-08
Ar	40	9.39e-23	1.03e-25	2.30e-27	8.63e-28	4.09e-27	8.38e-05
K	39	9.15e-03	7.66e-03	1.01e+02	2.72e+00	3.94e-01	3.65e-09
K	40	2.74e-12	9.73e-20	2.97e-90	8.69e-18	6.16e-18	2.16e-07
K	41	1.40e+01	2.68e-01	1.86e+03	3.32e+00	1.40e+00	3.54e-08
Ca	40	4.67e-01	2.36e-06	1.78e+00	4.32e-02	3.04e-03	2.10e-15
Ca	42	1.03e+02	1.69e+02	1.79e+04	3.96e+02	1.79e+02	2.04e-07
Ca	43	3.24e-01	5.24e-01	9.43e+03	8.45e+00	7.75e+00	2.54e-06
Ca	44	1.49e-01	3.61e+00	4.23e+03	1.32e+02	1.06e+01	3.37e-05
Ca	46	1.89e-17	3.99e-90	3.99e-90	2.84e-28	3.74e-28	5.85e+00
Ca	48	2.62e-22	7.27e-92	7.27e-92	7.27e-92	7.27e-92	3.67e+00
Sc	45	1.48e+00	1.89e+00	1.42e+03	1.10e+02	3.45e+01	7.43e-04
Ti	46	3.68e-02	3.04e-01	1.59e+02	9.69e+00	9.56e+01	3.03e-06
Ti	47	1.54e+00	1.74e+00	1.52e+03	3.76e+01	1.47e+01	3.32e-02
Ti	48	5.45e-01	9.96e-02	1.72e+03	4.28e+02	8.41e+01	2.17e-02
Ti	49	3.67e+00	5.74e-01	2.57e+02	1.32e+02	5.57e+01	3.26e+01
Ti	50	2.04e-04	2.26e-25	1.14e-28	8.19e-30	7.12e-17	1.28e+04
V	50	1.06e+01	1.33e-90	1.33e-90	1.31e-19	1.07e-17	3.93e+00

 This paper has been typeset from a \LaTeX file prepared by the author.